



Landy, J. C., Ehn, J. K., Babb, D. G., Thériault, N., & Barber, D. G. (2017). Sea ice thickness in the Eastern Canadian Arctic: Hudson Bay Complex & Baffin Bay. *Remote Sensing of Environment*, 200, 281-294.
<https://doi.org/10.1016/j.rse.2017.08.019>

Peer reviewed version

License (if available):
Other

Link to published version (if available):
[10.1016/j.rse.2017.08.019](https://doi.org/10.1016/j.rse.2017.08.019)

[Link to publication record in Explore Bristol Research](#)
PDF-document

This is the author accepted manuscript (AAM). The final published version (version of record) is available online via Elsevier at <http://www.sciencedirect.com/science/article/pii/S0034425717303887?via%3Dihub>. Please refer to any applicable terms of use of the publisher.

University of Bristol - Explore Bristol Research

General rights

This document is made available in accordance with publisher policies. Please cite only the published version using the reference above. Full terms of use are available:
<http://www.bristol.ac.uk/pure/about/ebr-terms>

1 **Sea ice thickness in the Eastern Canadian Arctic: Hudson Bay Complex**
2 **& Baffin Bay**

3
4 Jack C. Landy^{1,2*}; Jens K. Ehn¹; David G. Babb¹; Nathalie Thériault¹; David G. Barber¹

5
6 ¹ Centre for Earth Observation Science, Riddell Faculty of Environment Earth and Resources,
7 University of Manitoba, Winnipeg, Canada.

8 ² Bristol Glaciology Centre, School of Geographical Sciences, Faculty of Sciences, University of
9 Bristol, Bristol, United Kingdom

10
11 * *Corresponding Author: Jack Landy, Centre for Earth Observation Science, University of Manitoba,*
12 *125 Dysart Road, Winnipeg, Manitoba, Canada, R3T 2N2.*

13 *Now at: Bristol Glaciology Centre, 12 Berkeley Square, Bristol, Somerset, United Kingdom, BS8 1SS*

14 *Tel: 1-204-232-6113, Email: umlandy@cc.umanitoba.ca | jclandy@gmail.com*

15
16 **Keywords:** Sea ice thickness, Eastern Canadian Arctic, ICESat, Cryosat-2, sea ice deformation, ocean
17 freshwater budget

18 **Abstract**

19 Past observations of sea ice thickness in the Eastern Canadian Arctic (ECA) have generally been
20 restricted to drill-hole measurements at a few local sites on landfast ice. Here we use data from the laser
21 altimeter ICESat and the radar altimeter Cryosat-2 to present a 14-year record (2003-2016) of high-
22 resolution and spatially extensive ice thickness observations for the ECA and identify 12 sub-regions
23 with distinct patterns. The mean sea ice growth rate within the seasonally ice-covered ECA from
24 November to April is 23 cm mo^{-1} ($565 \text{ km}^3 \text{ mo}^{-1}$), with the fastest increase in thickness occurring through
25 strong ice convergence and deformation in eastern Hudson Bay and Foxe Basin. Our results demonstrate
26 characteristically asymmetrical distributions of sea ice thickness in both Hudson Bay and Baffin Bay,
27 but in opposing directions. In Hudson Bay the spring ice cover is 40 cm thicker in the eastern region
28 compared to the northwestern region, whereas in Baffin Bay the ice is 20 cm thicker in the western half
29 of the bay compared to the eastern half. In Hudson Bay we find that years with strong and positive ice
30 drift vorticity (i.e. cyclonic and convergent conditions) correlate with increasingly asymmetrical sea ice
31 covers, with the level of west-east asymmetry varying from 2 to 11 cm per 100 km. However, in Baffin
32 Bay the ice drift vorticity is typically negative (i.e. anticyclonic and divergent) with no obvious link to
33 the asymmetry of the spring ice cover. Finally, we estimate that large interannual variations in spring sea
34 ice volume within the ECA lead to $\pm 15\%$ variations in the volume of freshwater available at the ocean
35 surface during summer.

36

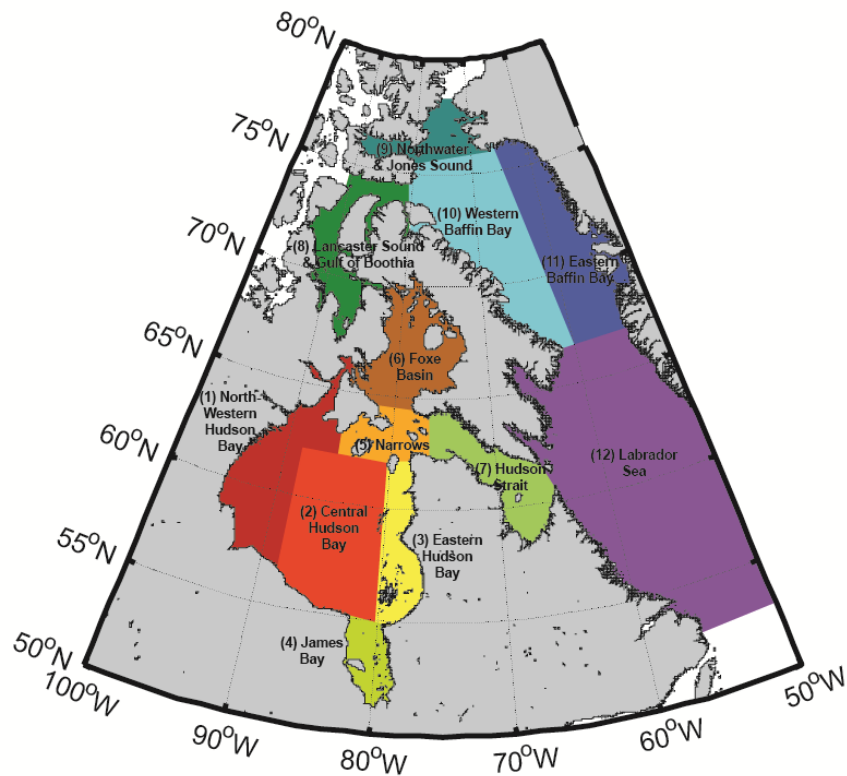
37 **1. Introduction**

38 Not only has the summertime area of Arctic sea ice declined over the past few decades (Comiso 2012),
39 but recent studies have demonstrated that the thickness of the ice cover has also been significantly
40 reduced since the turn of the century (Kwok and Rothrock 2009), (Kwok et al. 2009), (Laxon et al. 2013),
41 (Kwok and Cunningham 2015). Regular and spatially extensive sea ice thickness observations are
42 important for a number of reasons, including: estimating the volume of the Arctic sea ice cover (Kwok
43 and Cunningham 2015); validating numerical sea ice models (Schweiger et al. 2011); estimating the
44 freshwater flux entering the ocean following summer melt and downstream effects of this flux on oceans
45 at lower latitudes (Granskog et al. 2011; Morison et al. 2012); evaluating marine mammal habitat, for
46 instance polar bear migration routes (Regehr et al. 2007); and forecasting marine transportation (shipping
47 or cruise) routes (Stewart et al. 2010); among many others. Recent advances in satellite altimetry are
48 overcoming the considerable challenges involved with obtaining regional sea ice thickness estimates.
49 Most studies have focused on the central Arctic sea ice pack, while there have been few published
50 observations of sea ice thickness at lower latitudes, for example in the Eastern Canadian Arctic (ECA),
51 which is a region of significant importance for the global freshwater cycle. In this study, we use satellite
52 altimeter measurements of sea ice freeboard to provide the first long-term (decadal) estimates for sea ice
53 thickness and volume over the entire ECA.

54 The ECA consists of several seasonally ice-covered water bodies, including the two largest: Hudson Bay
55 and Baffin Bay. Hudson Bay is a large inland subarctic sea that is isolated from open ocean circulation
56 and therefore acts as a relatively independent system from the Atlantic and Arctic Oceans (Stewart and
57 Barber 2010). The larger area of the Hudson Bay Complex (HBC) refers to Sub-Regions SR1-7 (Figure
58 1) defined in this study. Currents in the HBC are primarily wind-driven and cyclonic, affected only by

59 cold-water intrusions through relatively small openings in the north via Fury and Hecla Straits and
60 northeast via Hudson Strait (Hochheim and Barber 2010). In contrast, Baffin Bay (SR10-11) is
61 continuously affected by Arctic Ocean water flowing into the bay through Nares Strait and Lancaster
62 Sound, as well as cycling with Atlantic water across Davis Strait through the Baffin Island & West
63 Greenland Currents. Mean circulation in Baffin Bay is cyclonic, with stronger currents in summer and
64 fall than in winter and spring, but a southward counter-current on the Greenland Shelf contributes to
65 strong horizontal shears in the eastern region of the bay (Tang et al. 2004).

66



67

68 **Figure 1.** Twelve sub-regions of the Eastern Canadian Arctic.

69

70 The sea ice cover within the ECA generally undergoes one full freeze-thaw cycle each year. There is
71 typically no multi-year ice in the HBC, whereas Baffin Bay retains a small portion while some multi-
72 year ice is imported into the bay from the central Arctic Ocean through Nares Strait (SR9) (Kwok 2005).
73 Across the ECA ice formation progresses from the northwest to the southeast (Stern and Heide-Jørgensen
74 2003) (Gagnon and Gough 2005) with a two-month delay between freeze-up in Foxe Basin (SR6) and
75 the Labrador Sea (SR12). Studies have linked significant declining trends in ECA sea ice concentration
76 (from 5% to 9% decade⁻¹ (Parkinson and Cavalieri 2008)), to increasing surface air temperatures (SATs),
77 particularly in the spring and fall (Tang et al. 2004) (Hochheim and Barber 2010) (Hochheim, Lukovich,
78 and Barber 2011). These results are supported by observations of later fall freeze-up in the northern
79 region of Hudson Bay and in Baffin Bay, but earlier melt onset in James Bay (SR4) and the Labrador
80 Sea in recent decades (Gagnon and Gough 2005) (Stroeve et al. 2014).

81 The few observational studies of sea ice thickness in the Hudson Bay Complex have been restricted to *in*
82 *situ* drill-hole measurements at seven sites on landfast first-year ice around the coast prior to 2003.
83 Average winter maximum ice thickness has been estimated from these sites as approximately 0.9 to 2.4
84 m (Gagnon and Gough 2006). From the same dataset (Gough, Gagnon, and Lau 2004) identified east-
85 west asymmetry in the long-term trends in ice thickness between approximately 1960 and 2000, with ice
86 thickening (+0.1-1.5 cm yr⁻¹) on the western side of Hudson Bay (SR1), but thinning (-0.5-0.8 cm yr⁻¹)
87 on the eastern side (SR3) (Gagnon and Gough 2006). Numerical modelling studies of sea ice in the HBC
88 provide simulated estimates for the average winter maximum ice thickness ranging from around 1 to
89 >2.5 m, although these studies disagree on the spatial distribution of sea ice (Wang, Mysak, and Ingram
90 1994), (Saucier et al. 2004), (Joly et al. 2011). Ice thicknesses in Baffin Bay and the Labrador Sea are
91 highly variable. For instance, (Valeur et al. 1996) combined restricted ice thickness measurements with

92 a thermodynamic sea ice model to demonstrate that annual maximum ice thickness decreases from 1.75
93 m at the coast of Baffin Island in the northwest to <0.75 m in the southeast. Freshwater budgets have
94 indicated that 20-90% more ice is produced in the ECA than estimated by concurrent *in situ* ice thickness
95 data (Prinsenberg 1988) (Prinsenberg and Peterson 2003), because these data fail to account for the
96 contribution of pressure ridges in the upper tail of the ice thickness distribution. In summary, observations
97 of sea ice thickness in the ECA are extremely sparse and typically more than a decade out-of-date, and
98 model predictions are not validated with sufficient observations nor agree on the regional distribution of
99 the ice cover.

100 The thickness distributions within the ECA are significantly affected by the presence of coastal polynyas.
101 In particular, a large polynya has been observed to form occasionally throughout the winter and spring
102 in the northwestern region of Hudson Bay (SR1) e.g. (Gough, Gagnon, and Lau 2004); often triggered
103 by the smaller Roes Welcome Sound Polynya (Barber and Massom 2007). A second large, persistent
104 polynya forms in the North Water, at the northern end of Baffin Bay and Jones Sound (SR9), during most
105 years in spring (Tang et al. 2004). Both of these features are thought to principally be latent-heat
106 polynyas. The NW Hudson Bay Polynya is caused by strong offshore westerly winds opening up areas
107 of water along the northwestern coast and enhancing ice production (Saucier et al. 2004). The North
108 Water Polynya is caused by an ice arch which forms in Kane Basin and limits the influx of ice from the
109 Arctic Ocean, in conjunction with a heat flux from upwelling of the West Greenland Current (Melling,
110 Gratton, and Ingram 2001). The ice covers within both of these polynyas are generally thin, intermittent
111 or absent. Sea ice that grows thermodynamically is continuously exported by winds to the south and east
112 in Hudson Bay and to the south in Baffin Bay.

113 With the arrival of NASA's ICESat mission, operational from 2003 to 2008, and ESA's Cryosat-2
114 mission, from 2010 until present, satellite altimetry has become the preeminent technique for acquiring
115 high temporal and spatial resolution remote estimates of Arctic sea ice thickness. Total snow plus sea ice
116 freeboard can be obtained from ICESat by calculating the height difference between laser echoes from
117 the sea surface (e.g. from leads between ice floes) and echoes from the snow surface. On the other hand,
118 only sea ice freeboard is obtained from Cryosat-2 because the radar wave theoretically penetrates the
119 snowpack. Snow depth, snow density and sea ice density must be estimated or parameterized to convert
120 ice freeboard to thickness, following Archimedes' principle, e.g. (Kwok and Rothrock 2009), (Laxon et
121 al. 2013). Ice thickness can generally be retrieved with an uncertainty <0.5 m (Ricker et al. 2014). By
122 applying this technique, past studies have been able to document the long-term decline in sea ice volume
123 within the Arctic Ocean during the 2000s (Kwok and Rothrock 2009). Interannual variations in Arctic
124 ice volume have also been detected, including for instance the severe loss in 2007 (Maslanik et al. 2007)
125 and minor rebound in 2013 and 2014 (Tilling et al. 2015). However, past studies have commonly
126 truncated their observations above a latitude of 70° , because the satellite orbital coverage is sparser and
127 the existing snow climatology is invalid at lower latitudes. Instead they have focused only on the central
128 Arctic Ocean and neglected lower latitude Arctic seas such as Hudson Bay and Baffin Bay.

129 Here we utilize altimeter observations of sea ice freeboard from ICESat and Cryosat-2, complimented
130 with thin-ice thickness observations from the SMOS L-band radiometer, to derive a near-continuous 14-
131 year record of sea ice thickness in the entire Eastern Canadian Arctic, from 2003 to 2016. In Section 2
132 we outline the procedures used to process raw laser/radar echoes and obtain sea ice freeboard, as well as
133 our methods to estimate snow depth and parameterize snow and sea ice densities. We introduce an error
134 budget that can be used to analyze the uncertainty of the retrieved ice thickness estimates. In Section 3

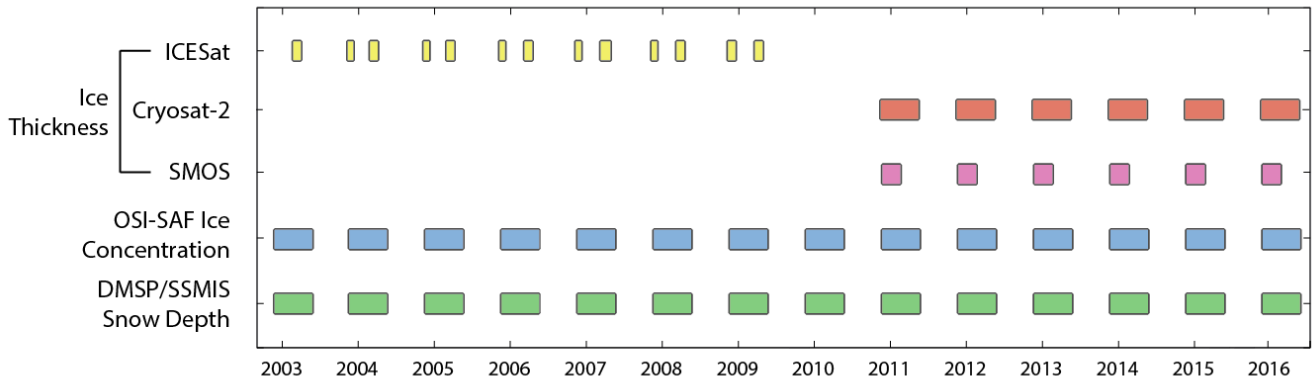
135 we analyze decadal trends and interannual variability in sea ice thickness and volume within several
136 regions of the ECA (Figure 1). In Section 4 we evaluate whether observed interannual variability in
137 Hudson Bay and Baffin Bay ice thickness distributions can be explained by patterns of ice motion, and
138 discuss the implications of our results for the freshwater budget of the ECA. Finally, in Section 5 we
139 conclude our findings and outline potential avenues for future research.

140

141 **2. Data and Methods**

142 Various methods for estimating sea ice thickness from satellite observations have been outlined in
143 previous studies, for ICESat (Forsberg and Skourup 2005), (Kwok et al. 2007), (Kwok and Cunningham
144 2008), (Farrell et al. 2009), (Kwok and Rothrock 2009); Cryosat-2 (Laxon et al. 2013), (Kurtz, Galin,
145 and Studinger 2014), (Ricker et al. 2014), (Kwok and Cunningham 2015), (Tilling et al. 2015); and
146 SMOS (Kaleschke et al. 2012), (Tian-Kunze et al. 2014). In this study we do not present substantial new
147 methods; rather we integrate and apply a selection of these published techniques with minor alterations
148 to an area not considered within previous studies. The temporal coverage of the satellite data used in the
149 study is illustrated in Figure 2. It is worth noting that while implementing our method we ensured that
150 the processing algorithms for ICESat and Cryosat-2 data were as close as possible, to prevent
151 inconsistencies or biases emerging between the two datasets. However, the algorithms were not identical
152 due to differences between the sensors, including footprint diameter, sampling interval, laser versus radar
153 altimeter, etc. Detailed descriptions of our methods for retrieving sea ice freeboard, sea ice thickness and
154 snow depth are provided in the supplementary materials.

155



156

157 **Figure 2.** Temporal coverage of the different satellite datasets used in this study.

158

159 **2.1. Satellite altimeter observations of sea ice freeboard**

160 The ICESat Geoscience and Laser Altimeter System (GLAS) was a profiling laser altimeter (wavelength
 161 1064 nm) which measured sea ice or snow-covered sea ice elevation above a reference Earth ellipsoid,
 162 with footprints ~70 m in diameter spaced at ~170 m intervals, up to a latitudinal limit of 86° (Kwok et
 163 al. 2006). The latest version of the ICESat GLAS data available at the time of analysis was Version 34
 164 of the Level 2 GLA05 & GLA13 products, available from the National Snow and Ice Data Center
 165 (NSIDC) at <http://nsidc.org/data/icesat/> (Zwally et al. 2014) from November to March, for the years
 166 2003-2008. Surface elevation (relative to the TOPEX/Poseidon ellipsoid) is determined by subtracting
 167 the range of a GLAS pulse from the height of the satellite above the earth, and is provided in the GLA13
 168 product following in-house waveform processing at NSIDC. For our study, valid elevation samples were
 169 obtained by filtering and correcting the raw data for known geodetic and oceanographic biases, including
 170 geoid undulations, tides, dynamic topography of the ocean and the inverted barometer effects (see

171 Supplementary Material 1). Sea ice and sea surface (lead) elevation samples were separated using an
172 adapted version of the approach of (Kwok et al. 2007) and (Kwok and Cunningham 2008), based on
173 differences in the reflective properties and relative elevation of these surface types. Sea ice freeboard
174 was calculated from the height difference between the ice surface elevation and sea level.

175 Cryosat-2 (CS-2) is a profiling radar altimeter (Ku-band) that theoretically penetrates snow if it is present
176 on sea ice, and measures the sea ice elevation above a reference ellipsoid. The footprint of CS-2 is pulse-
177 Doppler-limited ~300m along the track and pulse-limited ~1500 m across the track of the beam, with
178 samples spaced at ~300 m intervals, up to a latitudinal limit of 88° (Wingham et al. 2006). The latest
179 version of the CS-2 data available at the time of analysis was Baseline C of the Level 1B and Level 2,
180 SAR and (interferometric) SARIn data, accessed from the European Space Agency (ESA). Data were
181 available for November-April for each year between 2010-2016. Although data were also available for
182 May, the snow cover within the ECA generally begins to start melting during May which causes the
183 principal radar scattering surface (i.e. the altimeter's retracker range) to migrate up from the snow-ice
184 interface into the snowpack (Kwok 2014), biasing the ice thickness estimates. The assumption of full
185 radar penetration into the snowpack is discussed further in Supplementary Material 2. Surface elevation
186 can be determined by subtracting the range of a CS-2 pulse from the height of the satellite above the
187 earth. To obtain the range, we applied a 'retracking' correction to each empirical CS-2 waveform, based
188 on fitting a theoretical waveform function to the echo and then simple thresholding, following (Giles et
189 al. 2007), (Laxon et al. 2013) and (Kwok and Cunningham 2015) (see Supplementary Material 2). We
190 used only the power information in our analysis of SARIn echoes and truncated the waveforms from 512
191 to 128 bins before processing (Kurtz, Galin, and Studinger 2014). In this study we assumed that a
192 threshold of 70% of the echo power represented the mean scattering surface of the retracked fitted

193 waveform for both sea ice and leads, based on analysis of (Laxon et al. 2013), (Kurtz, Galin, and
 194 Studinger 2014) and (Ricker et al. 2014). Valid elevation samples were obtained by filtering and
 195 correcting the raw data for known geodetic and oceanographic biases. To ensure we maintained a
 196 consistent approach between ICESat and CS-2 processing methods, sea ice and sea surface (lead) radar
 197 waveforms were classified according to both their elevation and shape (backscattering) properties, using
 198 an adapted version of the approach of (Laxon et al. 2013; Kurtz, Galin, and Studinger 2014; Ricker et al.
 199 2014). Considerable detail on the design of the processing algorithms and techniques used to filter out
 200 waveforms from mixed surface ice/lead/open water/land types is provided in Supplementary Material 2.
 201 For instance, our filtering step included a series of dedicated algorithms to separate and classify pure
 202 waveforms from sea ice and leads. Sea ice freeboard was calculated from the height difference between
 203 the ice surface elevation and sea level. For verification purposes, we provide the raw winter (March)
 204 estimates for sea ice freeboard and distance of samples to their closest lead, separated for each satellite
 205 mission and between major regions of the ECA, in Table 1.

206

207 **Table 1.** Average March sea ice freeboard and distance of samples to their closest lead averaged
 208 separately over ICESat (2003-2009) and Cryosat-2 (2011-2016) periods. Note the ICESat freeboard is
 209 the total snow plus ice freeboard $h_{f_{total}}$ and the Cryosat-2 freeboard is only the ice freeboard without the
 210 snow wave-speed correction applied h_{f_i} .

Sea Ice Freeboard [m]		Distance to Closest Lead [km]	
ICESat	Cryosat-2	ICESat	Cryosat-2

Hudson Bay Complex (SR1-7)	0.231 ± 0.146	0.123 ± 0.121	23 ± 36	34 ± 43
Baffin Bay & Labrador Sea (SR9-12)	0.233 ± 0.156	0.106 ± 0.103	16 ± 30	42 ± 47

211

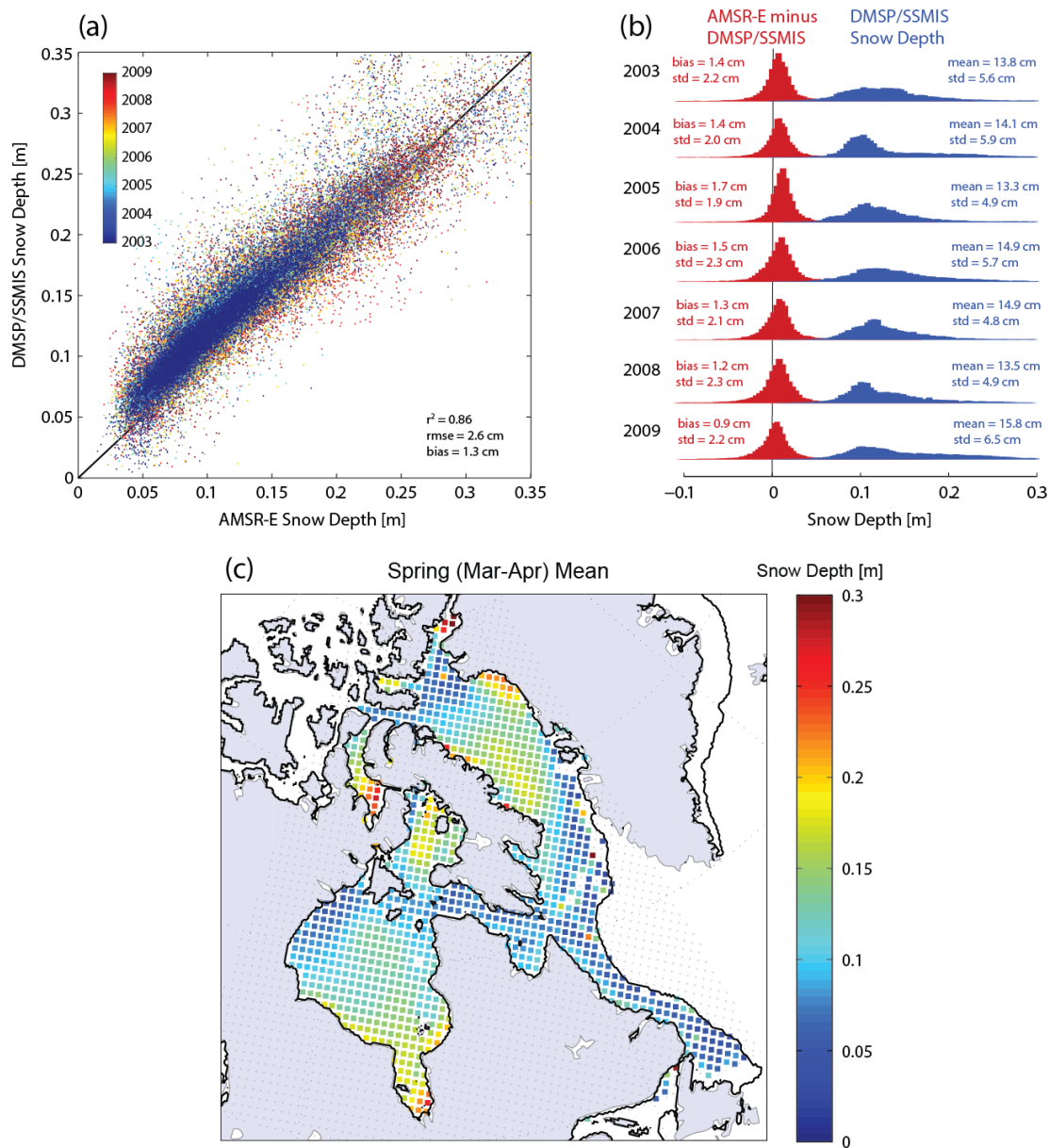
212 **2.2. Snow data**

213 To estimate sea ice thickness from freeboard, it is necessary to measure or parameterize the depth and
214 density of snow existing on the ice cover, as well as the densities of ice and seawater. Past studies have
215 generally used the ‘Warren climatology’, which is based on *in situ* snow measurements from Russian
216 drifting stations in the central Arctic Ocean (Warren et al. 1999). Since this climatology did not cover
217 our study area, we chose to reapply the technique of (Markus and Cavalieri 1998) to obtain snow depth
218 from DMSP/SSM/I-SSMIS brightness temperatures (25-km, available from NSIDC at
219 <http://nsidc.org/data/NSIDC-0001#>) (Maslanik and Stroeve 2016), which were available for 2003-
220 present (see Supplementary Materials 3). The coefficient of determination and RMSE between our 5-day
221 averaged snow depth estimates and those from resampled 25-km AMSR-E data, for December-May over
222 the concurrent period of observations 2003-2009, were 0.86 and 2.6 cm, respectively (Figure 3a). Figure
223 3b demonstrates that there are no anomalous biases between the datasets for individual years and that the
224 snow depth distribution was similar between years. Mean 2003-2016 spring snow depth is presented for
225 our study region in Figure 3c.

226 For snow density, we used a modified version (Kwok and Cunningham 2008) of the seasonally-varied
227 density observations provided in (Warren et al. 1999), but applied the same spatially-constant density for
228 all freeboard observations on a given day of year.

229

230



231

232 **Figure 3.** (a) Comparison between snow depth estimated from DMSP/SSMIS brightness temperatures
 233 (used in this study) and estimated from AMSR-E brightness temperatures (provided by NSIDC), over
 234 the concurrent period 2003-2009. (b) Histograms of annual mean snow depth from DMSP/SSMIS (blue)
 235 and difference between AMSR-E and DMSP/SSMIS snow depths (red) for 2003-2009. (c)

236 ‘Climatological’ mean snow depth in spring (March-April), from DMSP/SSMIS brightness
237 temperatures, for 2003-2016. The bold line gives the mean ice edge (20% ice concentration).

238

239 **2.3. Sea ice thickness & error budget**

240 Sea ice thickness h_i was estimated from ICESat freeboard observations using:

$$h_i = \left(\frac{\rho_w}{\rho_w - \rho_i} \right) h_{f_{total}} - \left(\frac{\rho_w - \rho_s}{\rho_w - \rho_i} \right) h_s, \quad (1)$$

241 where $h_{f_{total}}$ is the total ice plus snow freeboard, h_s is the snow depth, and bulk densities for sea ice ρ_i ,
242 snow ρ_s and seawater ρ_w provide the scaling for hydrostatic equilibrium. In contrast, sea ice thickness
243 was estimated from CS-2 freeboard observations using:

$$h_i = \left(\frac{\rho_w}{\rho_w - \rho_i} \right) h_{f_i} + \left(\frac{\rho_s}{\rho_w - \rho_i} \right) h_s, \quad (2)$$

244 where h_{f_i} is the ice-only freeboard, because the radar was assumed to penetrate the snow pack. A height
245 correction h_c was applied to the radar observations as follows: $h_{f_i} = h_{f_{radar}} + h_c$, before evaluating
246 Equation 2, to account for the lower wave propagation speed within the snowpack (Kwok and
247 Cunningham 2015). The correction is given by:

$$h_c = h_s \left(1 - \frac{c_s}{c} \right), \quad (3)$$

248 where c_s is the speed of light in snow, parameterized by $c_s = c(1 + 0.51\rho_s)^{-1.5}$ (Ulaby, Moore, and
249 Fung 1982). Snow density was obtained from W99 as described above, seawater density was taken as
250 1024 kg m^{-3} , and sea ice density was obtained from an ice thickness-dependent parameterization:
251 $\rho_i(h_i) = 936 - 18h_i^{0.5} \text{ kg m}^{-3}$, following (Kovacs 1996).

252 We attempted to approximate the random uncertainty σ of each ice thickness estimate by accounting for
253 individual uncertainties in: snow depth, snow density, sea ice density, seawater density, sea-surface
254 height (SSH) with respect to the geoid, radar speckle noise, and possible volume scattering of the CS-2
255 radar wave within the snowpack rather than from the snow-ice interface. Individual uncertainty
256 components are listed in Table S1 in Supplementary Materials 4 along with the references used, where
257 applicable. All components have fixed uncertainty, with the exceptions of the SSH and, in the case of
258 CS-2 measurements, the speckle noise and radar propagation uncertainty. Random uncertainties were
259 assumed to be uncorrelated and could therefore be combined, using Gaussian propagation of uncertainty,
260 to generate a single uncertainty estimate for each ICESat or CS-2 observation (Kwok and Cunningham
261 2008), (Ricker et al. 2014). However, for the majority of our analyses we gridded the ice thickness
262 measurements at a resolution of 50 km, using a mean filter inverse-linearly weighted by the sample
263 uncertainty and distance (Geiger et al. 2015). Thus gridded mean thickness uncertainty $\bar{\sigma}$ decreased
264 proportional to \sqrt{N} , where N is the number of samples. Samples with zero thickness (i.e. open water),
265 were removed prior to gridding. Minimum N was set at 10 samples, although the mean value of N for
266 the ICESat data was 191 and for the CS-2 data was 241.

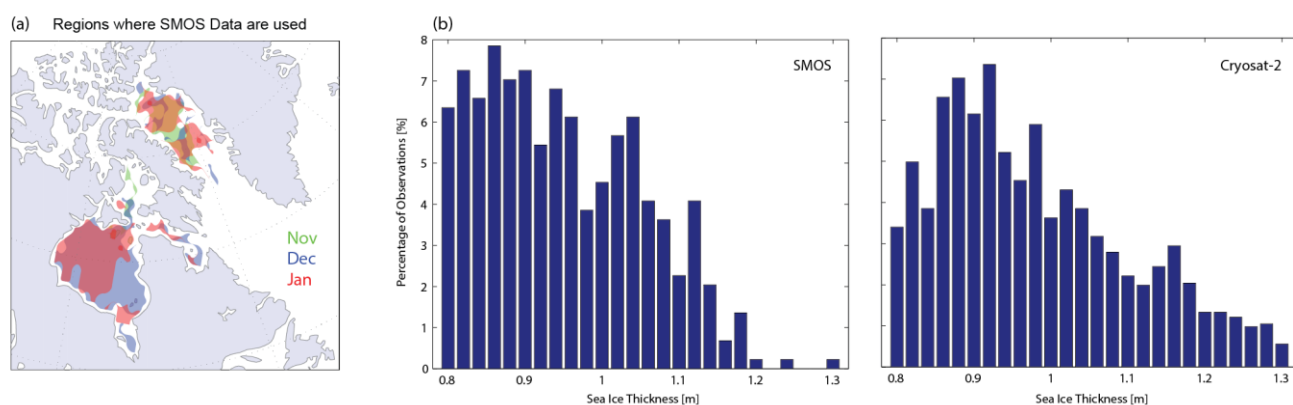
267

268 **2.4. Thin-ice thickness from SMOS**

269 Both the relative systematic and random uncertainties of altimeter-based ice thickness observations are
270 known to be higher in thinner ice e.g. (Ricker et al. 2014). For instance, the speckle noise in individual
271 Cryosat-2 samples places a lower limit on the reliably detectable ice thickness of approximately 0.5 m
272 (Kurtz, Galin, and Studinger 2014). Between November and January, the thickness of ice in the HBC
273 can often be below this limit (Gagnon and Gough 2006). We therefore obtained estimates of the thickness
274 of thin sea ice from the Soil Moisture and Ocean Salinity (SMOS) satellite (Kaleschke et al. 2012) to
275 integrate with the altimeter measurements. However, since SMOS data are only available for the CS-2
276 period: 2010-2016, we chose to only integrate these data between November and January, thereby
277 improving our estimates for ice thickness and volume in the fall and early winter months. Although this
278 prohibited us from analyzing ice thickness trends between ICESat and CS-2 data in November, we could
279 still analyze trends in March. We chose not to integrate the SMOS data between February and April,
280 because the average ice thickness in these months is typically much greater than 0.5 m.

281 Daily Level 3C SMOS thin ice thickness grids, with a resolution of 12.5 km, were obtained from the
282 Integrated Climate Data Center at the University of Hamburg (available at:
283 <http://icdc.zmaw.de/1/daten/cryosphere/l3c-smos-sit.html>) (Tian-Kunze, Kaleschke, and Maass 2013,
284 updated 2016). We calculated monthly average ice thickness from these daily estimates, for November
285 through January 2010-2015, using only data where both the thickness and uncertainty was ≤ 1 m.
286 However, the SMOS observations systematically underestimate the true ice thickness, potentially by 10s
287 of centimeters, because (1) ice with a true mean thickness > 1 m cannot be retrieved and (2) the algorithm
288 does not account for ice concentration $< 100\%$ (Tian-Kunze et al. 2014). Consequently, we calculated
289 monthly ice thickness as an average of SMOS and CS-2 observations in areas where the SMOS ice
290 thickness was ≤ 1 m (Figure 4a), but in the remaining ice-covered area used only CS-2 observations.

291 Figure 4a illustrates that the area of utilized SMOS data was largest in December, whereas in January the
 292 ice in regions such as Southeastern Hudson Bay began to thicken above 1 m and the SMOS data were
 293 omitted. The distributions of sea ice thickness from SMOS and CS-2 in the zone around the transition in
 294 validity between datasets (approximately 1 m) are very similar (Figure 4b). Both distributions show
 295 decreasing observations as the ice thickness increases from 0.9 up to 1.3 m, although there are less CS-2
 296 than SMOS observations for ice thickness <0.9 m because ice with a thickness approaching 0.5 m is less
 297 easily detected by CS-2.



298

299 **Figure 4. (a)** The areas where SMOS ice thickness data are utilized in November, December and January,
 300 averaged over the period 2010-2016. **(b)** Comparison between distributions of ice thickness from SMOS
 301 and Cryosat-2 within the transition zone in validity (0.8-1.3 m) between the two datasets.

302

303 2.5. Sea ice volume

304 A lack of spatially ubiquitous and consistent year-to-year ice thickness observations within each sub-
 305 region of the HBC presented a challenge for estimating changes in the volume of sea ice. Without

306 accounting for missing data, ice volume estimates obtained from an integral of ice thickness and
 307 concentration grids would be underestimated. To overcome this issue, we first interpolated the ice
 308 thickness grids using nearest-neighbour interpolation to fill small gaps; however, this technique could
 309 not reliably be used to fill gaps larger than 100 km. Thus, to calculate sea ice volume from the ice
 310 thickness observations within a sub-region we evaluated the following:

$$V_i = \Delta x^2 \left[\sum_{j=1}^{N_{usable}} (h_i C_i)_j + \bar{h}_i \sum_{j=1}^{N_{missing}} (C_i)_j \right], \quad (4)$$

311 where Δx is the grid cell size (50 km), N_{usable} and $N_{missing}$ are the number of usable and missing ice
 312 thickness grid cells, respectively, h_i is the ice thickness and C_i is the ice concentration within grid cell j ,
 313 and \bar{h}_i is the mean ice thickness within the region. Ice volume uncertainty was estimated by integrating
 314 the uncertainties in ICESat/CS-2 and SMOS data for the months November through January. Additional
 315 uncertainty involved with estimating the missing areas was then calculated as the standard deviation of
 316 h_i , for all months, weighted by the number of missing to usable grid cells. The mean fraction of usable
 317 ice thickness data: $N_{usable}/(N_{usable} + N_{missing})$, for all months studied, was 78%. The minimum
 318 fraction of usable data was 26%, with an equivalent uncertainty of $\pm 175 \text{ km}^3$ (16%), which occurred in
 319 November 2004 when sea ice concentration was low within the ECA. The maximum fraction of usable
 320 data was 97%, with an equivalent uncertainty of $\pm 68 \text{ km}^3$ (2%), which occurred in March 2006.

321

322 **2.6. Auxiliary data**

323 Sea ice concentration was obtained from the daily 12.5-km OSI-SAF global ice concentration
324 reprocessing dataset, available at <http://osisaf.met.no/p/ice/> (EUMETSAT 2015). Ice concentration data
325 were used to define the valid geographical area of altimeter observations, as described above.

326 Kinematic parameters of the Hudson Bay and Baffin Bay sea ice motion fields were derived from weekly
327 25-km Polar Pathfinder sea ice motion vectors (Version 3, available from NSIDC at:
328 <http://nsidc.org/data/NSIDC-0116>) (Tschudi et al. 2016). Unambiguous drift vectors were only available
329 in areas >25 km from the coastline. Mean ice drift speed and direction were obtained for select time
330 periods from the product of vertical u and horizontal v component vectors. We also calculated the
331 velocity component in the west-east direction across Hudson Bay, i.e. from northwestern (sub-region,
332 SR1) to eastern (SR5) Hudson Bay (Figure 1), to examine whether ice drift affects spatial variations in
333 the Hudson Bay ice thickness distribution. By tracking the ice drift vectors across the boundaries between
334 sub-regions 1, 2 and 5, we could estimate the mean speed of ice moving into or out of each region.
335 Finally, the kinematic parameters: ice divergence, vorticity and shear, were calculated following (Kwok
336 2001) (details in Table 4), which characterize deformation within the ice pack.

337

338 **3. Results**

339 **3.1. Regional distribution of sea ice thickness**

340 Maps of the ‘climatological’ mean sea ice thickness in both fall (Nov-Dec) and spring (Mar-Apr), over
341 the full data period 2003-2016, are illustrated in Figure 5. The seasonal cycle of the ice thickness within
342 different regions of the ECA is summarized in Table 2. The fall pattern of ice thickness reflects the north

343 to south progression of freeze-up within the HBC and Baffin Bay, with the thickest ice located in the
 344 Northwater & Jones Sound (1.01 ± 0.53 m; SR9) and Foxe Basin ($\bar{h}_i = 0.70 \pm 0.44$ m; SR6). The thinnest
 345 ice is located in the partially frozen Eastern Hudson Bay (0.13 ± 0.09 m; SR3), James Bay (0.25 ± 0.18
 346 m; SR4) and in the Labrador Sea (0.38 ± 0.37 m; SR12). The ice cover in the ECA experiences rapid
 347 growth between November and February (average of 25-40 cm mo⁻¹) before slowing (5-20 cm mo⁻¹)
 348 thereafter. However, the average growth rate is 15 cm mo⁻¹ (80%) higher in the Hudson Bay Complex
 349 (SR1-7) than in Baffin Bay and the Labrador Sea (SR9-12). Throughout winter the thickest sea ice is
 350 found in Foxe Basin, which has an average maximum thickness of 1.99 ± 1.33 m in spring, whereas after
 351 January the thinnest ice is located in Eastern Baffin Bay (SR11), which has the lowest maximum
 352 thickness of 1.00 ± 0.61 m.

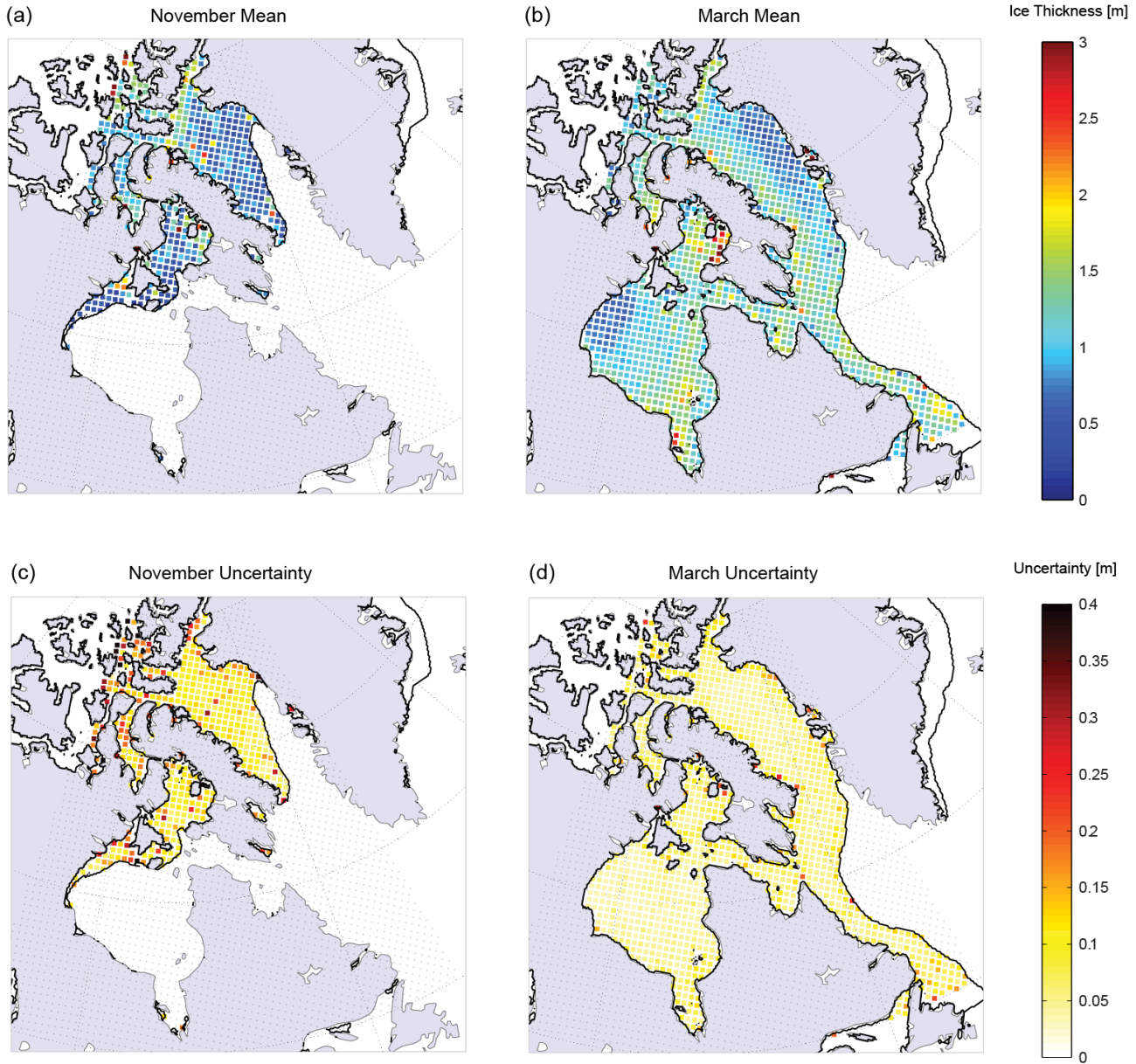
353

354 **Table 2.** Seasonal sea ice thickness [m] averaged over the period 2003-2016 within twelve sub-regions
 355 of the Eastern Canadian Arctic. Estimates for Nov-Jan combine ICESat GLAS, Cryosat-2 and SMOS
 356 data, whereas estimates for Feb-Apr combine only the altimeter datasets. Change in ice thickness per
 357 month [m mo⁻¹] is provided in the final row.

Sea Ice Thickness [m]												
Region	1	2	3	4	5	6	7	8	9	10	11	12
Nov	0.28	0	0	0.06	0.14	0.60	0.12	1.11	1.09	0.70	0.49	0.28
Dec	0.39	0.44	0.25	0.45	0.51	0.81	0.46	1.30	0.93	0.83	0.51	0.48
Jan	0.90	0.93	0.84	0.79	0.80	1.40	0.77	1.40	1.15	0.75	0.61	0.60
Feb	1.03	1.15	1.35	1.65	1.22	1.70	1.29	1.46	1.47	1.28	0.87	1.49

Mar	1.09	1.25	1.41	1.66	1.26	1.86	1.49	1.48	1.72	1.22	0.97	1.35
Apr	1.25	1.44	1.67	1.44	1.43	2.12	1.59	1.66	1.57	1.18	1.03	1.35
$m\ mo^{-1}$	0.20	0.28	0.35	0.33	0.26	0.32	0.31	0.10	0.15	0.12	0.12	0.25

358



359

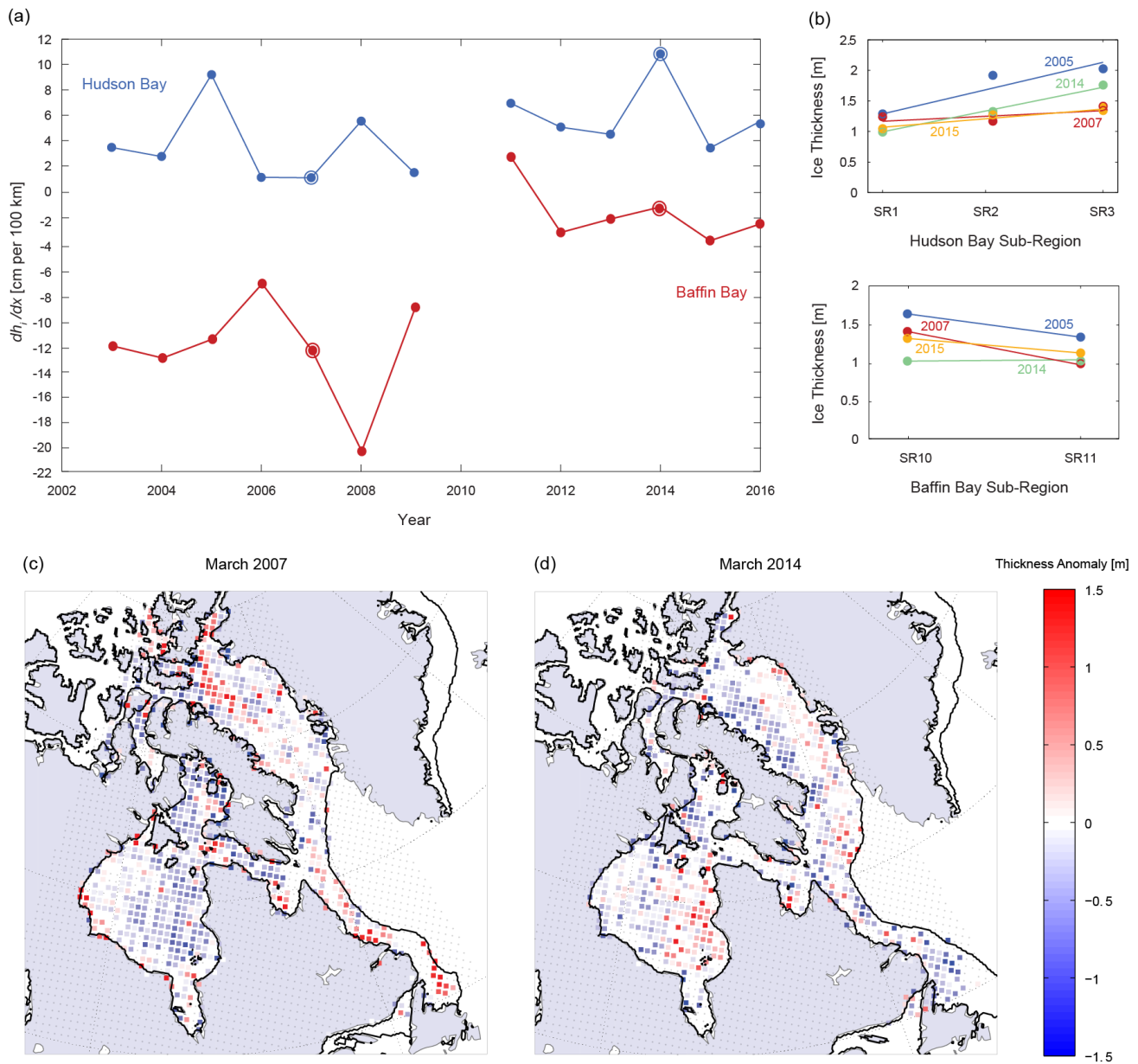
360 **Figure 5.** ‘Climatological’ (a) mean sea ice thickness and (c) average uncertainty in thickness, as
361 observed by ICESat GLAS, Cryosat-2 and SMOS in November, and (b) mean sea ice thickness and (d)
362 average uncertainty in thickness, as observed by ICESat GLAS and Cryosat-2 in March, for 2003-2016.
363 Bold lines give the mean ice edge (20% ice concentration) for these periods.

364

365 The average random uncertainties are generally higher in fall ($\bar{\sigma} = 0.15$ m; 33%) than in spring ($\bar{\sigma} = 0.08$
366 m; 6%), due to the bias associated with CS-2 data when the ice is very thin and the higher uncertainty
367 associated with the SMOS data used between November and January (Figure 5). The minimum random
368 uncertainty of gridded altimeter observations in spring is 0.03 m, typical of most of Hudson Bay and
369 large areas of Baffin Bay and the Labrador Sea. Uncertainty is higher in coastal areas and smaller bays,
370 including Foxe Basin, Hudson Strait and James Bay, where sea surface variability was characteristically
371 higher and only SARIn CS-2 data (with higher speckle noise) were available (Figure 5d).

372 East-west asymmetry in mean spring ice thickness is evident across both Hudson and Baffin Bays, but
373 in opposing directions (Figure 5b). There is a gradual increase in thickness from 1.17 m in Northwestern
374 Hudson Bay (SR1) to 1.34 m in Central Hudson Bay (SR2) and finally to 1.54 m in Eastern Hudson Bay
375 (SR3). This supports the existing hypothesis that sea ice in Hudson Bay has a characteristic northwest-
376 to-southeast asymmetry in thickness (Saucier et al. 2004), (Gagnon and Gough 2006), (Joly et al. 2011).
377 In contrast, spring ice thickness decreases from 1.20 m in Western Baffin Bay (SR10) to 1.00 m in
378 Eastern Baffin Bay (SR11). This also supports past observations that sea ice in Baffin Bay has a
379 characteristic east-to-west asymmetry in thickness (Valeur et al. 1996).

380



381

382 **Figure 6.** Interannual variations in the east-west asymmetry of spring sea ice thickness in the Eastern
 383 Canadian Arctic: (a) variations in the asymmetry parameter $d\bar{h}_1/dx$ in Hudson Bay and Baffin Bay from
 384 2003 to 2016, and (b) asymmetries across the two bays in four years. Spatial anomalies of March ice
 385 thickness in the Eastern Canadian Arctic with respect to the climatological average in (c) a close-to-
 386 symmetrical year in Hudson Bay but asymmetrical year in Baffin Bay, 2007, and (d) a particularly

387 asymmetrical year in Hudson Bay but close-to-symmetrical year in Baffin Bay, 2014. Bold lines give the
388 mean ice edge (20% ice concentration).

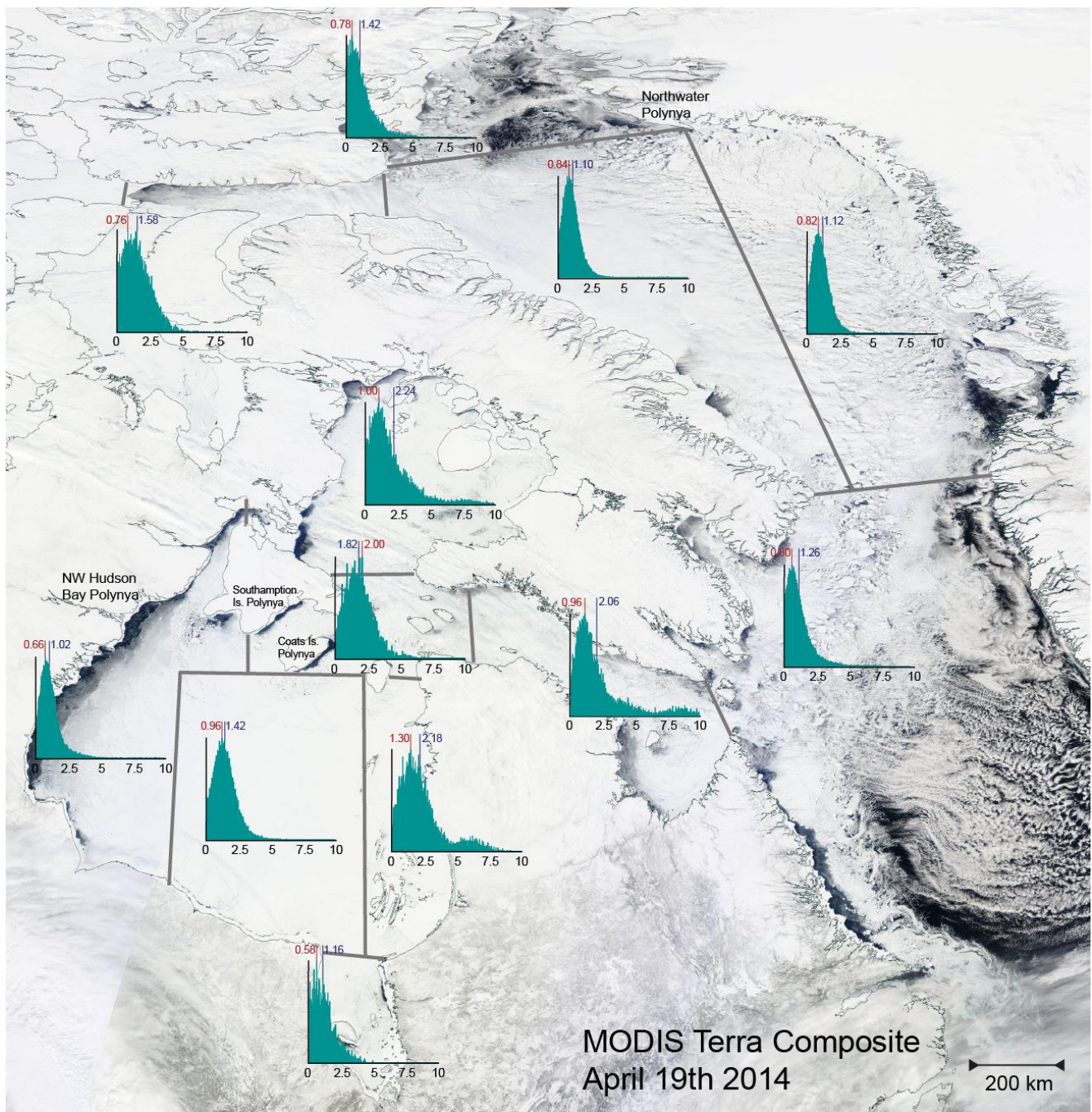
389

390 To evaluate whether these characteristically asymmetrical ice thickness distributions occur every year,
391 and whether the strength of the asymmetry varies between years, we calculated an asymmetry parameter
392 for each spring between 2003 and 2016. The parameter $d\bar{h}_i/dx$ was calculated from the change in mean
393 thickness across the ~750 km distance from SR1 to SR3 in Hudson Bay or the ~300 km distance from
394 SR10 to SR11 in Baffin Bay. Figure 6a shows that the parameter clearly varies on an interannual basis,
395 while Figure 6b shows that a significant portion of this variability can be attributed to variability in ice
396 thickness in Eastern Hudson Bay (SR3) and Western Baffin Bay (SR10). There is also an apparent shift
397 in the Baffin Bay ice thickness distribution from strongly asymmetrical during the ICESat period (2003-
398 2008) to weakly asymmetrical during the CS-2 period (2011-2016). The reliability of this observation,
399 as well as potential implications of the shift, will be discussed in more detail in Section 3.2. Figures 5c-
400 d demonstrate two years with distinctive and opposing spring ice thickness anomaly distributions in the
401 ECA. For instance, the west-east asymmetry was particularly strong (11 cm per 100 km) in Hudson Bay
402 but weak (-1 cm per 100 km) in Baffin Bay in 2014 (Figure 6d and 5). Conversely, in 2007 negative ice
403 thickness anomalies in Central and Eastern Hudson Bay led to very little change in ice thickness (1 cm
404 per 100 km) across Hudson Bay, but positive anomalies in Western Baffin Bay led to strong ice thickness
405 asymmetry across Baffin Bay (Figure 6c). Although spring ice thickness asymmetry contrasted between
406 the two bays during these years, we found no significant correlation or anti-correlation between Hudson
407 Bay and Baffin Bay asymmetry parameters over the study period.

408 Areas of thin ice are observed during spring in known polynya locations, such as in North Western
409 Hudson Bay, in the Northwater, and around Southampton, Coats and Mansel Islands in the Hudson Bay
410 Narrows (SR5). While Northwestern Hudson Bay is among the first regions of the ECA to freeze-up
411 during fall (Figure 5a) (Gagnon and Gough 2005) and the ice grows rapidly during November, December
412 and January (0.31 m mo^{-1}), it contains the thinnest sea ice of any region within the Hudson Bay Complex
413 between February and April, coinciding with a 65% reduction in the ice growth rate (0.11 m mo^{-1}). This
414 lends support to the hypothesis that the Northwestern Hudson Bay polynya acts as an ‘ice factory’, where
415 ice grows thermodynamically before it is exported to the south and east by winds, precluding the
416 development of thick ice. It has been suggested that a significant amount of ice in the HBC cannot be
417 accounted for within models without the existence of this polynya (Prinsenber 1988). For example,
418 there was a large opening of the northwestern Hudson Bay polynya during April 2014 (Figure 7).
419 Looking at ice thickness distributions for Sub-Regions 1-3 during this month we find a strong west to
420 east gradient in the modal ice thickness from 0.6 to 1.4 m. Furthermore, there is a thick, clearly
421 dynamically-grown secondary peak between 4-8 m in Eastern Hudson Bay. This feature is the result of
422 ice being dynamically deformed as it is pushed up against the eastern boundary of Hudson Bay. Extended
423 tails with secondary modes are also observed in the distributions for Hudson Strait, Foxe Basin and to a
424 lesser extent in the Narrows, while there are essentially no extended tails in Northwestern and Central
425 Hudson Bay, and James Bay, indicating very little dynamic thickening in these regions. The secondary
426 mode of thick ice in the Foxe Basin distribution helps to explain why this region contains the thickest ice
427 within the ECA in spring (Table 2), despite other regions having higher latitude.

428

429



430

431 **Figure 7.** Regional variations in the frequency distribution of sea ice thickness across the Eastern
 432 Canadian Arctic in April 2014, superimposed on a composite of MODIS *Terra* images acquired on April
 433 19th. The locations of persistent polynyas are indicated, including the Northwestern Hudson Bay Polynya

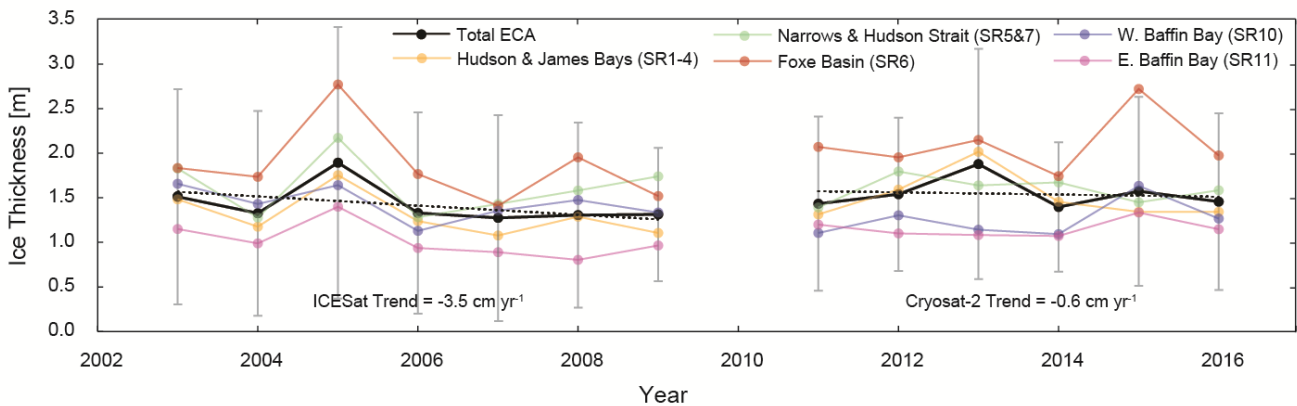
434 and the Northwater Polynya. Normalized frequency distributions of ice thickness have a 5-cm bin spacing
435 and the mean and modal ice thickness are given in purple and red, respectively.

436 Extended tails are not present within the April 2014 ice thickness distributions for Baffin Bay and the
437 Labrador Sea (SR10-12). However, there is a slight extended tail present within the Northwater and Jones
438 Sound (SR9) which we attribute to thick multi-year ice entering Baffin Bay from the central Arctic
439 through Nares Strait (Kwok 2005). Overall, at least in 2014, it appears that the ice pack within Baffin
440 Bay underwent very little dynamic thickening and was predominantly the result of *in situ* thermodynamic
441 ice growth.

442

443 3.2. Interannual variability of sea ice thickness and volume

444



445

446 **Figure 8.** Time-series of mean March sea ice thickness in the Eastern Canadian Arctic from 2003 to
447 2016, for the entire ECA and for groups of sub-regions separately. Error bars indicate one standard
448 deviation around the mean total ECA ice thickness. Linear trends are presented as separate dashed lines

449 for the mean ice thickness during ICESat and Cryosat-2 data periods, although neither is statistically
450 significant.

451

452 Time-series of March ice thickness for the total ECA, and for five groups of sub-regions, are shown in
453 Figure 8. Over the study period, the average end-of-winter ice thickness for the entire ECA varied from
454 a low of 1.08 m in 2007 to highs of 1.72 m in 2005 and 1.55 m in 2013. The 2013 anomaly is primarily
455 due to thicker ice in the HBC, while ice thickness in Western and Eastern Baffin Bay varied little from
456 other years during 2013. The sea ice cover was particularly thick in 2005, with a relative peak in ice
457 thickness evident in all nine sub-regions, excluding Northwestern Hudson Bay which exhibited less
458 interannual variability than other regions throughout the study period. This observed thickening
459 coincided with a particularly strong overall thickening of the Arctic first-year ice cover in 2005 (Kwok
460 et al. 2009). Variations in the standard deviation of ice thickness observations (error bars in Figure 8)
461 illustrate that it is not only the mean thickness but also the ice thickness distribution that changes between
462 years. For instance, the standard deviations of ice thickness in March 2005, 2013 and 2015 were more
463 than 80% higher than those in March 2009 and 2014. This observation further supports the notion that
464 ice dynamics play a key role in shaping the frequency distribution of ice thickness in the Eastern
465 Canadian Arctic (Figure 7; see Section 4.1). Trends in sea ice thickness were negative over the entire
466 study period (Figure 8), although decreasing from -3.5 cm yr^{-1} ($p = 0.21$) during the ICESat record to
467 -0.5 cm yr^{-1} ($p = 0.89$) during the CS-2 record. The monthly-averaged sea ice volume increases in all sub-
468 regions of the ECA over the ice growth season, with a net production of $565 \text{ km}^3 \text{ mo}^{-1}$ (Table 3). Within
469 the Hudson Bay Complex (SR1-7) ice volume increases at an average rate of $328 \text{ km}^3 \text{ mo}^{-1}$. The highest
470 growth rate of $486 \text{ km}^3 \text{ mo}^{-1}$ occurs during January as the remaining portions of Southeastern Hudson

471 Bay freeze-up and thermodynamic growth accelerates in Northwestern Hudson Bay with cooling
 472 temperatures. We observe a decline in the ice volume between March and April in James Bay, which is
 473 likely caused by earlier melt onset relative to the greater HBC (Markus, Stroeve, and Miller 2009).
 474 Around 28% of the spring ice volume within the HBC is contained within Central Hudson Bay (SR2),
 475 which has the highest rate of ice production ($94 \text{ km}^3 \text{ mo}^{-1}$). However, despite having an area almost one
 476 third the size of SR2, Eastern Hudson Bay (SR3) still contributes 13% of the spring ice volume within
 477 the HBC, due to its long tail of dynamically thickened ice (Figure 6).

478

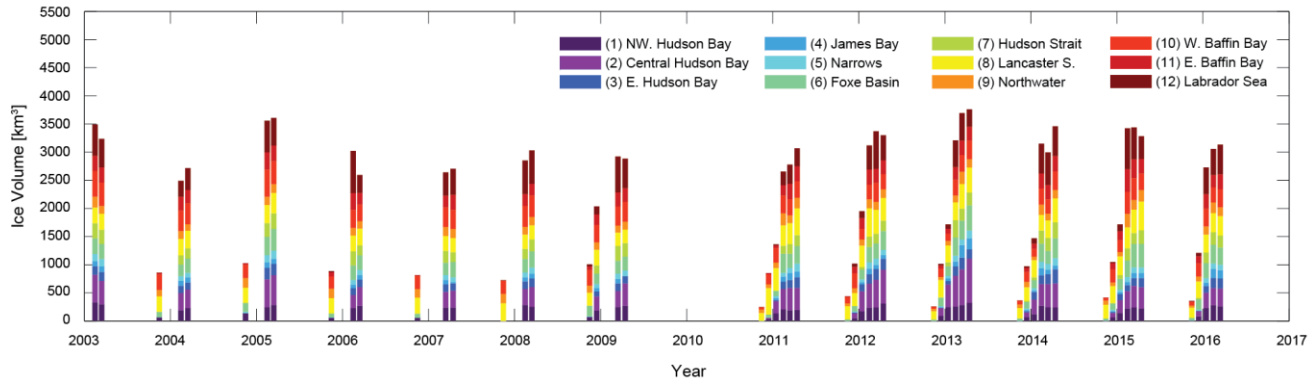
479 **Table 3.** Seasonal sea ice volume [km^3] averaged over the period 2003-2016 within twelve sub-regions
 480 of the Eastern Canadian Arctic. The area [10^3 km^2] of each sub-region is also provided. Estimates for
 481 November and December combine ICESat GLAS, Cryosat-2 and SMOS data, whereas estimates for
 482 January-April combine only the altimeter datasets. The rate of ice production per month [$\text{km}^3 \text{ mo}^{-1}$] is
 483 provided in the final row.

Region	Sea Ice Volume [km^3]											
	1	2	3	4	5	6	7	8	9	10	11	12
Area	275	333	128	63	90	183	178	253	125	310	303	1,160
Nov	36	0	0	2	6	75	2	231	92	152	23	10
Dec	82	108	22	15	27	127	36	305	82	222	98	46
Jan	184	289	95	40	50	172	72	311	94	205	142	150
Feb	249	349	148	94	99	241	189	328	127	347	213	508
Mar	252	397	159	103	104	285	213	332	162	342	254	500
Apr	256	471	173	89	115	341	221	394	147	316	259	425

km³ 48 94 38 22 24 54 50 26 16 38 49 108
 mo⁻¹

484

485



486

487 **Figure 9.** Time-series of sea ice volume in the Eastern Canadian Arctic from 2003 to 2016. Ice volume
 488 estimates for Nov-Jan 2010 to 2015 were obtained from combined Cryosat-2 and SMOS ice thickness
 489 data.

490

491 In the Baffin Bay Complex (SR9-12) ice volume increases at an average rate of 211 km³ mo⁻¹, although
 492 the highest growth rate of 604 km³ mo⁻¹ occurs in February, a month later than in Hudson Bay. This is
 493 because the southern parts of Baffin Bay and Labrador Sea only start to freeze-up in January-February,
 494 when air temperatures reach their annual minimum (Tang et al. 2004). The significant loss of ice volume
 495 (-75 km³ mo⁻¹) in the Labrador Sea between March and April (Table 3) can be attributed to stronger
 496 southward ice export than replenishment from Baffin Bay and Hudson Strait (Valeur et al. 1996).

497 The seasonal progression of ice volume within the ECA can be observed from the combined CS-2 and
 498 SMOS data for 2010-2016 in Figure 9. Sea ice is generally only present in restricted portions of Hudson

499 Bay and Baffin Bay, as well as Foxe Basin, Lancaster Sound & the Gulf of Boothia and the Northwater
500 & Jones Sound, in November and December. Significant ice production occurs in Eastern Hudson Bay
501 & James Bay, Hudson Strait, and Baffin Bay & the Labrador Sea between January and March. By
502 focusing on a few sub-regions independently, it is noticeable that ice volume appears to occasionally
503 decrease between successive months. For instance, ice volume in Hudson Strait dropped by 20-70 km³
504 between February and March in 2013 and 2014. Within Northwestern Hudson Bay, the Narrows, Hudson
505 Strait and the Northwater the decrease in ice volume can be explained by the formation of polynyas along
506 the coast and areas of open water within the ice pack (e.g. Figure 7). In Hudson Bay these polynyas are
507 maintained by northwesterly winds that advect the existing ice cover eastwards (Section 4.1).

508

509 **4. Discussion**

510 **4.1. Role of ice dynamics in shaping the Hudson and Baffin Bay ice thickness distributions**

511 The characteristically asymmetrical east-west distributions of sea ice thickness in Hudson Bay and Baffin
512 Bay during spring (Figure 5b) suggest that ice dynamics could play an important role in shaping the ice
513 cover in both of these regions. For instance, end-of-spring ice thickness is around 0.5-1.0 m in
514 Northwestern Hudson Bay, while in contrast in Eastern Hudson Bay it is generally 1.5-2.0 m, with several
515 zones >2 m. This implies that in the former the ice is mainly thermodynamically grown and thus relatively
516 young (Granskog et al. 2011) and that significant dynamic redistribution of thinner floes into thicker ice
517 occurs in the latter (Prinsenberg 1988). Dynamic ice redistribution is driven by the deformation of and
518 between drifting ice floes, such that kinematic parameters of the ice motion field (divergence, vorticity
519 and/or shear) could explain, at least partially, interannual variations in Hudson Bay and Baffin Bay ice

520 thickness asymmetry. December to April averages of these parameters (i.e. for the total ice growth
521 season) within Hudson Bay, for each year with ICESat or CS-2 observations, are presented in Table 4.

522 **Table 4.** Mean kinematic parameters of the ice motion field in Hudson Bay (SR1-3) between December
 523 and April for all coinciding years with ICESat-2 and Cryosat-2 observations. Years with exceptionally
 524 asymmetrical east-west ice thickness distributions are highlighted in red and exceptionally level
 525 thickness distributions in blue.

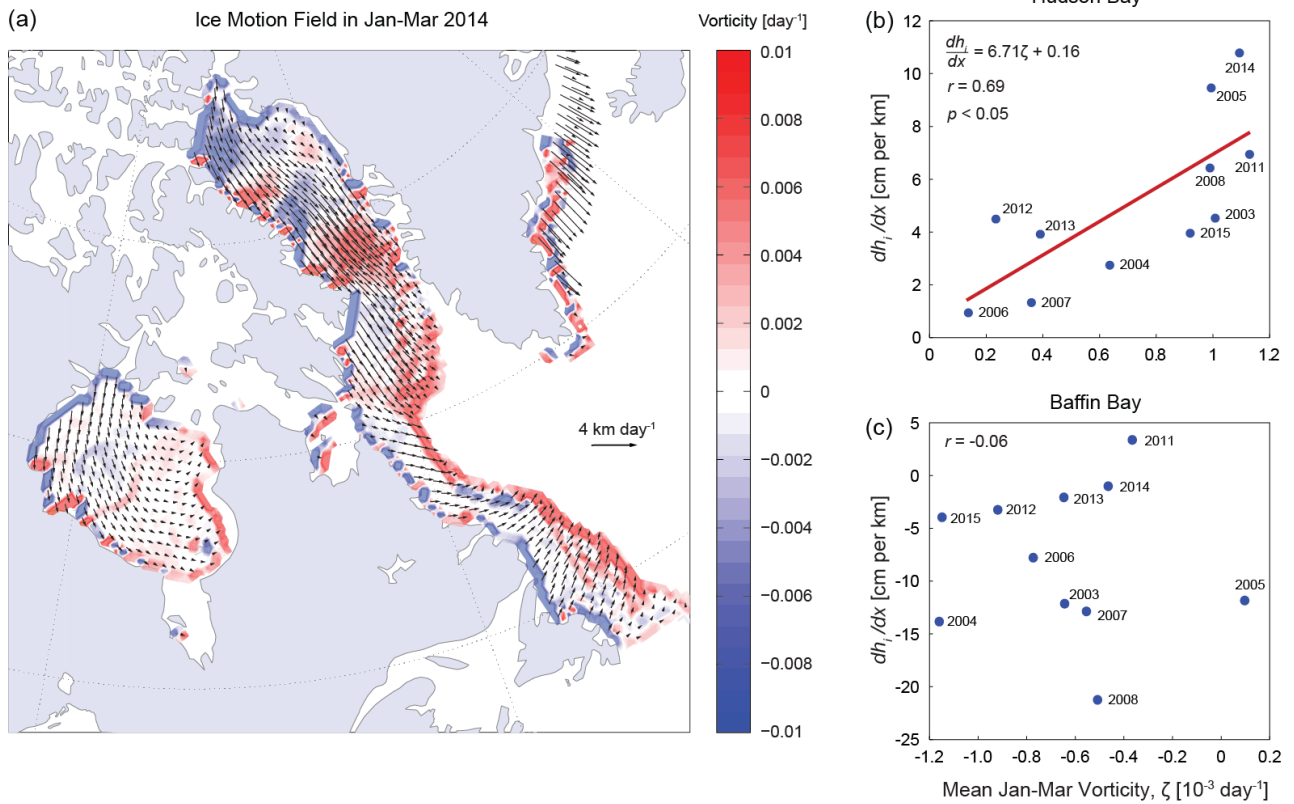
	Speed [km day ⁻¹]	Direction (° from N)	W-E Velocity [km day ⁻¹]	Divergence [10 ⁻³ day ⁻¹]	Vorticity [10 ⁻³ day ⁻¹]	Shear [10 ⁻³ day ⁻¹]
	$\sqrt{u^2 + v^2}$		$(u, v)_{east}$	$\frac{(u_x + v_y)}{2}$	$\frac{(v_x - u_y)}{2}$	$\sqrt{\frac{(u_x - v_y)^2}{2} + \frac{(u_y - v_x)^2}{2}}$
2003	1.45	126	0.74	0.48	0.91	12.7
2004	1.38	123	0.83	0.57	0.59	12.2
2005	1.37	123	0.81	0.60	0.90	11.7
2006	1.14	136	0.51	0.92	0.16	12.1
2007	1.24	128	0.75	0.82	0.35	12.8
2008	1.31	117	0.81	0.53	0.90	11.5
2011	1.50	111	1.21	0.38	1.02	12.1
2012	0.88	116	0.64	0.00	0.24	11.1
2013	1.03	122	0.72	0.82	0.38	13.7
2014	1.63	114	1.24	0.50	0.99	12.9
2015	1.52	111	1.12	0.22	0.84	11.3
Ave	1.31	121	0.85	0.53	0.66	12.19

526

527 In Hudson Bay, the mean ice drift speed for the December-April period is 1.31 km day⁻¹ in a southeast
 528 direction (121°), with a mean west-east drift velocity of 0.85 km day⁻¹ (Table 4). All yearly December-

529 April west-east drift velocities are positive, reflecting the fact that mean drift directions do not vary
530 considerably from southeast (ranging from 111 to 136°). The units of the kinematic parameters are day⁻¹,
531 because they characterize (unitless) meter per meter deformation of the ice pack; however, average
532 divergence and vorticity are more than an order of magnitude smaller than shear. Mean ice vorticity is
533 above zero in every year, consistent with the predominantly cyclonic ice motion in Hudson Bay (Figure
534 10a) and convergence of the ice pack (Hochheim, Lukovich, and Barber 2011). Finally, the mean ice
535 drift velocities into (+) or out of (-) sub-regions 1, 2 and 3 over the full study period are -0.53, +0.30 and
536 +0.55 km day⁻¹, respectively. This observation is aligned with sea ice being characteristically exported
537 from Northwestern Hudson Bay after it forms, whereupon it drifts east into central Hudson Bay and
538 converges in Eastern Hudson Bay. As originally suggested in Section 3.2, this would explain the
539 secondary mode of very thick ice in the 2014 eastern Hudson Bay thickness distribution (Figure 7) and
540 the west-east asymmetry in the spring mean ice thickness (Figure 5b).

541 In Baffin Bay, the mean ice drift speed for the December-January period is 4.03 km day⁻¹, more than
542 three times the speed of ice drift in Hudson Bay, in a south-southeast direction (147°). Given the
543 predominantly southward drift of ice in Baffin Bay, the mean west-east drift velocity of 1.78 km day⁻¹
544 represents a smaller fraction of total ice transport than it did in Hudson Bay. In contrast to Hudson Bay,
545 the vorticity in Baffin Bay is negative in every year of the study period, with the exception of 2005
546 (Figure 10c), which indicates predominantly anticyclonic ice motion and divergence of the ice pack.
547 Indeed, average values for the divergence parameter between December and April are approximately
548 four times higher in Baffin Bay than in Hudson Bay over the study period. Since ice motion is typically
549 not from the west to the east and is generally divergent, dynamic ice motion occurring within the bay
550 likely cannot explain the west-east asymmetry of ice thickness in Baffin Bay.



552

553 **Figure 10.** (a) Mean sea ice motion and vorticity fields in the Eastern Canadian Arctic between January
 554 and March 2014; relationship between vorticity ζ and the ice thickness asymmetry parameter dh_i/dx in
 555 (b) Hudson Bay and (c) Baffin Bay, for the period 2003-2015.

556

557 To examine the relationship between interannual variations in sea ice motion/deformation and thickness
 558 within Hudson Bay, we recursively calculated the correlation coefficient between each of the six
 559 parameters in Table 4 and the east-west ice thickness asymmetry parameter dh_i/dx (Figure 6a), using
 560 varying time intervals to average the kinematic parameters. We discovered that the ice drift direction,

561 the west-east component of the ice drift velocity vector $(u, v)_{east}$ and the vorticity ζ are all significantly
562 correlated with $d\bar{h}_i/dx$, particularly over the time period from the start of January to the end of March.
563 Figure 10b illustrates the relationship between the asymmetry and ice vorticity ($r = 0.69$, $p < 0.05$). A
564 higher vorticity clearly produces a more asymmetrical (i.e. more convergent) ice cover in Hudson Bay,
565 which is illustrated in Table 4. However, we found no relationship between vorticity and ice cover
566 asymmetry in Baffin Bay (Figure 10c).

567 The mean ice motion field between January and March 2014 demonstrates that strong cyclonic ice drift
568 leads to negative vorticity (ice divergence) along the coast of Northwestern Hudson Bay and positive
569 vorticity (ice convergence) along the opposite coast in Eastern Hudson Bay (Figure 10a). Interestingly,
570 the zone of positive vorticity around the Belcher Islands also coincides with particularly high spring ice
571 thickness in 2014 (Figure 6d). Most of the years studied fit the linear relationship relatively well (Figure
572 10b); however, the Hudson Bay ice covers in 2004 and 2015 were less asymmetrical than expected, based
573 on the vorticity, whereas the ice covers in 2005, 2012 and 2014 were more asymmetrical than expected.
574 This implies that factors other than ice dynamics also influence interannual variations in the asymmetry
575 of the Hudson Bay sea ice thickness distribution. Overall, the winter-spring ice vorticity can explain just
576 under half (48%) of the variance in the asymmetry of the spring Hudson Bay ice thickness distribution.
577 This emphasizes the strong role of ice vorticity in regulating the Hudson Bay ice cover, building on the
578 results of (Hochheim, Lukovich, and Barber 2011) who showed that positive ice vorticity also contributes
579 to negative spring sea ice extent anomalies, particularly in northern Hudson Bay. However, we found
580 only a weak ($r = 0.25$) insignificant relationship between January-March ice vorticity and spring sea ice
581 volume.

582 Sea ice persisted unusually late into the summer in July 2015, with heavy ice conditions in Eastern
583 Hudson Bay cutting off some communities in Northern Quebec from resupply shipments. It seems
584 intuitive that thicker ice at the end of spring may contribute to such conditions in summer; however, the
585 ice cover in spring 2015 was not uncharacteristically asymmetrical as it was in 2014 or thick as it was in
586 2005. In fact, we found no clear spatial relationship between the end-of-spring ice thickness distribution
587 and sea ice concentration anomalies in summer.

588

589 **4.2. Summer freshwater fluxes**

590 The freshwater content of Hudson Bay varies as a function of sea ice formation/melt, seasonal changes
591 in river input, precipitation/evaporation, and the rate of freshwater export through Hudson Strait. River
592 discharge contributes an estimated 630-870 km³ yr⁻¹ freshwater to Hudson and James Bays, which
593 corresponds to 12% of the total pan-Arctic runoff (Saucier et al. 2004), (Lammers et al. 2001), and the
594 net product of precipitation (snow and rain) minus evaporation contributes 220 km³ yr⁻¹ (St-Laurent et
595 al. 2011). In contrast, outflow through Hudson Strait removes an estimated 800-1050 km³ yr⁻¹ freshwater
596 from the basin (Saucier et al. 2004), (St-Laurent et al. 2011). Baffin Bay is less well protected from
597 neighbouring water masses than Hudson Bay. Therefore, the freshwater content of Baffin Bay also varies
598 as a function of sea ice formation/melt, seasonal changes in river and glacial ice input, and
599 precipitation/evaporation, but most importantly freshwater import/export through northern channels
600 including Lancaster Sound, Jones Sound and Davis Strait, as well as through Davis Strait to the south.
601 Precipitation in Baffin Bay is low, contributing only 30 km³ yr⁻¹, and glacial ice contributes an estimated
602 500 km³ yr⁻¹ (assuming half of the ice melts in the bay) (Tang et al. 2004). The freshwater imported from

603 the northern channels is approximately $920\text{-}1460 \text{ km}^3 \text{ yr}^{-1}$, whereas the volume exported through Davis
 604 Strait is approximately $3700 \text{ km}^3 \text{ yr}^{-1}$ (Tang et al. 2004). In addition, around $1200 \text{ km}^3 \text{ yr}^{-1}$ of freshwater
 605 is transported northward into Baffin Bay from the Labrador Sea on the Greenland Shelf (Cuny, Rhines,
 606 and Kwok 2005). Our observations of sea ice volume allow us to evaluate the remaining component of
 607 the freshwater budgets in Hudson and Baffin Bays, i.e. the removal of freshwater from the ocean as sea
 608 ice forms in fall and subsequent re-entry to the surface mixed-layer as the ice melts in summer (Landy et
 609 al. 2014), albeit potentially in a different location than where it formed.

610 We developed a climatology of summer/fall (July-October) sea surface salinity in the Eastern Canadian
 611 Arctic from 36-km Aquarius observations (available at: http://nsidc.org/data/AQ3_SSS) (Brucker,
 612 Dinnat, and Koenig 2015), collected over the period 2011-2014. Surface salinity varied from 25 to 35
 613 psu between different areas of the ECA. These data were then used to estimate the bulk salinity of sea
 614 ice forming from the seawater, according to the following ice thickness-dependent salinity
 615 parameterization (Ryvlin 1974):

$$S_i = S_w(1 - S_R)e^{-\phi\sqrt{h_i}} + S_R S_w, \quad (5)$$

616 where S_w is the sea surface salinity (from Aquarius observations), S_R is the ratio of the bulk salinity at
 617 the end of the ice growth season to standard seawater, taken as 0.175 (Tian-Kunze et al. 2014), and ϕ is
 618 a growth rate coefficient taken as 0.5 (Ryvlin 1974). The volume of freshwater stored in the ice was
 619 estimated from:

$$V_{fw} = V_i \left(1 - \frac{S_i}{33}\right) \left(\frac{\rho_i}{\rho_w}\right). \quad (6)$$

620 The reference salinity of seawater in Hudson Bay was taken as 33 psu, following (St-Laurent et al. 2011).
621 Uncertainty in the volume of freshwater was calculated by propagating errors in ice volume and sea
622 surface salinity observations through Equations 5 and 6.

623 Regional variations in the climatological average (2003-2016) volume of freshwater stored in the ECA
624 at the end of spring (April) are provided in Table 5. The volume of freshwater removed from the ocean
625 through ice formation within the Hudson Bay Complex (SR1-7) reaches a maximum of $1253 \pm 15 \text{ km}^3$
626 by the end of April. This volume identifies the peak freshwater stored in sea ice before melt onset in
627 May. In Hudson and James Bays, average April V_{fw} stored in the ice cover is $742 \pm 10 \text{ km}^3$, which is
628 approximately 100 km^3 higher than the model prediction of (St-Laurent et al. 2011). This supports the
629 assertion of (Prinsenbergh 1988) that typical estimates for the freshwater content of Hudson Bay miss the
630 contribution from the very thick tail-end of the ice thickness distribution, i.e. from pressure ridges, which
631 is included in our observations. The volume of freshwater stored within the sea ice cover in Baffin Bay
632 (SR10-11) reaches a maximum of $445 \pm 5 \text{ km}^3$ by the end of April, which is similar to the estimated total
633 annual export of ice through Davis Strait (Cuny, Rhines, and Kwok 2005). The freshwater volume per
634 unit area (yield) which can potentially be expelled to the ocean during summer ice melt is largest in Foxe
635 Basin at 1.41 m, since the thickest ice within the ECA is found in this region, whereas it is smallest
636 Northwestern Hudson Bay, Western Baffin Bay and the Labrador Sea at 0.70, 0.62 and 0.32 m,
637 respectively (Table 5). However, this assumes that the ice cover melts *in situ* and is not redistributed
638 across the bay while it melt between April and July.

639 When integrated over the entire Hudson Bay Complex, the thickness of this fresh meltwater ‘layer’ varies
640 from a low of 0.82 m in 2011 to a high of 1.15 m in 2005, corresponding to -10% and +27% of the 2003-
641 2016 average, respectively. The anomalously high freshwater volume stored within the Hudson Bay ice

642 cover in 2005 may explain the strong sea ice melt but weak river water signals present during fall 2005
 643 in Central Hudson Bay, as observed by (Granskog et al. 2011). Indeed, the volume of freshwater
 644 contained within the ice cover in SR2 at the end of spring 2005 was $>100 \text{ km}^3$ higher than the long-term
 645 average (Table 5). When integrated over Baffin Bay, the thickness of the fresh meltwater layer varies
 646 with a similar magnitude to the Hudson Bay Complex, from a low of 0.62 m in 2014 to a high of 0.88 m
 647 in 2005, corresponding to -14% and +22% of the 2003-2016 average, respectively. The respective
 648 standard deviations of the volumes of freshwater stored in the Hudson Bay Complex and Baffin Bay ice
 649 covers are 171 and 51 km^3 .

650

651 **Table 5.** An estimate of the volume of freshwater [km^3] stored (-) in the sea ice cover at the end of spring
 652 (April) and the depth of pure freshwater [m] expelled (+) to the ocean following summer melt (assuming
 653 ice melts *in situ*), for the period 2003-2016, within twelve sub-regions of the Eastern Canadian Arctic.

Region	1	2	3	4	5	6	7	8	9	10	11	12
Spring FW stored [km^3]	-192	-352	-130	-68	-88	-257	-166	-304	-122	-257	-188	-371
Summer FW layer [m]	0.70	1.06	1.02	1.07	0.97	1.41	0.93	1.20	0.98	0.83	0.62	0.32

654

655 One implication of these strong interannual variations in freshwater storage is that the volume of
 656 freshwater available during summer for outflow to the Labrador Sea varies between years (Myers,
 657 Akenhead, and Drinkwater 1990), (St-Laurent et al. 2011). The sensitivity of the freshwater budget to
 658 interannual variations in spring sea ice volume can be calculated by assuming constant estimates for river

659 discharge, glacial ice input, precipitation minus evaporation, and total inflow/outflow from neighbouring
660 water masses, as outlined above. We estimate that the available summer freshwater varies by $\pm 14\%$
661 depending on interannual variations in the volume of the Hudson Bay Complex ice cover and by $\pm 16\%$
662 depending on variations in the Baffin Bay ice cover. This could have significant repercussions for
663 stratification, water mass properties and productivity downstream in the Labrador Sea (Déry et al. 2011),
664 (Granskog et al. 2011).

665

666 **5. Conclusions**

667 In this study we have presented a climatology of sea ice thickness observations in the Eastern Canadian
668 Arctic for the period 2003-2016, bridging the sampling intervals of the laser altimeter ICESat and the
669 radar altimeter Cryosat-2. Very few in situ ice thickness observations exist for the ECA that would allow
670 us to elucidate thickness patterns and trends. Our satellite-derived results demonstrate that sea ice
671 thickness is characteristically asymmetrical in both Hudson and Baffin Bays, but in opposing directions.
672 The spring ice cover is 40 cm thicker in northwestern compared to eastern Hudson Bay, and 20 cm thicker
673 in western compared to eastern Baffin Bay. However, the level of west-east asymmetry varies
674 considerably on an interannual basis, ranging from 2 to 11 cm per 100 km in Hudson Bay and from -21
675 to 2 cm per 100 km in Baffin Bay. In spring, the thinnest ice is located in Eastern Baffin Bay ($\bar{h}_i = 1.00$)
676 and in Northwestern Hudson Bay ($\bar{h}_i = 1.17$), where a large and persistent polynya frequently develops.
677 The thickest ice ($\bar{h}_i = 1.99$) is located in Foxe Basin, where ice formation begins early in fall and ice
678 dynamics contribute to extending the upper tail of the ice thickness distribution. By integrating the ice
679 thickness observations with ice concentration data, we calculated that the mean sea ice growth rate within
680 the Eastern Canadian Arctic from November to April is $565 \text{ km}^3 \text{ mo}^{-1}$, with the ice thickening most

681 rapidly in Eastern Hudson Bay (where strong convergence encourages dynamic growth and ridging).
682 Several latent heat polynyas within the ECA, specifically in Northwestern Hudson Bay, may not contain
683 thick ice by the end of winter but still contribute significantly to the overall ice production.

684 By examining kinematic parameters of the ice motion field within Hudson Bay, we found a statistically
685 significant positive relationship between the January-March vorticity of the ice pack and the spring ice
686 thickness asymmetry ($r = 0.69$). Increasingly positive vorticity indicates cyclonic ice motion and
687 convergence of ice within the bay. Based on this relationship, a 20% increase in vorticity enhances the
688 ice thickness asymmetry by approximately 1 cm per 100 km in the west to east direction. Winter ice
689 vorticity is generally negative in Baffin Bay, which indicates anticyclonic ice motion and divergence of
690 ice within the bay, and perhaps as a consequence we found no statistical relationship between the vorticity
691 and spring ice thickness asymmetry. The combined altimeter datasets also appear to show that the ice
692 thickness distribution in Baffin Bay has become progressively less asymmetrical over the past decade
693 due, in particular, to declining sea ice thickness on the western side of the bay.

694 Finally, our results suggest that the freshwater yield during summer from melting sea ice would be
695 highest in Foxe Basin (around 1.4 m) and lowest in Northwestern Hudson Bay, Eastern Baffin Bay and
696 the Labrador Sea (0.3-0.7 m). However, owing to strong interannual variations in spring ice volume, the
697 depth of the freshwater layer at the ocean surface in summer, after all the sea ice has melted, can vary by
698 tens of centimeters. The implication of this variability is that the volume of freshwater within the Eastern
699 Canadian Arctic available for outflow south through the Labrador Sea during summer varies by an
700 estimated $\pm 15\%$ between years.

701 The prospective launch date for the next major satellite altimeter with a focus on the polar regions is
702 ICESat-2 in 2017. Data from this satellite could be used to extend the sea ice thickness record presented

703 in this study to 15-20 years, which would enable a more robust statistical evaluation of the ice thickness
704 and volume patterns identified here and potentially long-term trend analysis. Negative trends in ice
705 thickness continuing into the coming decades would undoubtedly influence socioeconomic activities in
706 the ECA. Vessel traffic has more than doubled over the past ten years as thick sea ice has disappeared
707 from the Canadian Arctic and the open water season has lengthened (PEW Charitable Trust April 2016).
708 A thinner ice pack throughout the ECA will not only contribute to the continued lengthening of the open
709 water shipping season, but also draw the attention of parties interested in year round shipping to
710 communities and mine sites throughout the ECA. One of the primary northern marine transportation
711 corridors identified by the Canadian Coast Guard is located between the Labrador Sea and the Port of
712 Churchill in Hudson Bay. High-resolution ice thickness observations, such as those presented here, could
713 be used to examine whether interannual variations and/or long-term changes in the quantity of ice at the
714 thickest (>3 m) end of the ice thickness distribution have affected shipping along this and other
715 transportation corridors in the Eastern Canadian Arctic.

716

717 **Acknowledgements**

718 This work is a contribution to the Natural Sciences and Engineering Research Council of Canada
719 (NSERC) Collaborative Research and Development (CRD) project: BaySys (contributions of climate
720 change and hydro-electric regulation to the variability and change of freshwater-marine coupling in the
721 Hudson Bay system), undertaken in collaboration with Manitoba Hydro, to ArcticNet Networks of
722 Centres of Excellence (NCE), and to the Arctic Science Partnership (ASP) asp-net.org. Funding for JCL,
723 DB and NT was provided by NSERC, ArcticNet NCE, and the Canada Research Chair (CRC) program.
724

725 **References**

- 726 Barber, D.G. and R.A. Massom 2007. “The Role of Sea Ice in Arctic and Antarctic Polynyas.” Pp. 1-54
727 in *Polynyas: Windows to the World*, edited by W.O. Smith and D.G. Barber. Elsevier Oceanography
728 Series.
- 729 Brucker, L., E. Dinnat, and L. Koenig. 2015. “Aquarius L3 Weekly Polar-Gridded Sea Surface Salinity,
730 Version 5.” Distributed Active Archive Center, Boulder, Colorado USA.
- 731 Comiso, J. 2012. “Large Decadal Decline of the Arctic Multiyear Ice Cover.” *J. Climate* 25:1176-1193.
- 732 Cuny, J., P.B. Rhines, and R. Kwok. 2005. “Davis Strait volume, freshwater and heat fluxes.” *Deep Sea*
733 *Res. Part 1: Ocean. Res. Papers* 52(3):519-542.
- 734 Déry, S.J., T.J. Mlynowski, M.A. Hernández-Henríquez, and F. Straneo. 2011. “Interannual variability
735 and interdecadal trends in Hudson Bay streamflow.” *J. Mar. Sys.* 88(3):341-351.
- 736 EUMETSAT. 2015. “Global sea ice concentration reprocessing dataset 1978-2015, v1.2.” Norwegian
737 and Danish Meteorological Institutes.
- 738 Farrell, S.L., S.W. Laxon, D.C. McAdoo, D. Yi, and H.J. Zwally. 2009. “Five years of Arctic sea ice
739 freeboard measurements from the Ice, Cloud and land Elevation Satellite.” *J. Geophys. Res.* 114:C04008.
- 740 Forsberg, R. and H. Skourup. 2005. “Arctic Ocean gravity, geoid and sea-ice freeboard heights from
741 ICESat and GRACE.” *Geophys. Res. Lett.* 32:L21502.
- 742 Gagnon, A.S. and W.A. Gough. 2005. “Trends in the Dates of Ice Freeze-up and Breakup over Hudson
743 Bay, Canada.” *Arctic* 58(4):370-382.
- 744 Gagnon, A.S. and W.A. Gough. 2006. “East-west asymmetry in long-term trends of landfast ice thickness
745 in the Hudson Bay region, Canada.” *Clim. Res.* 32:177-186.
- 746 Geiger, C., H.R. Müller, J.P. Samluk, E.R. Bernstein, and J. Richter-Menge. 2015. “Impact of spatial
747 aliasing on sea-ice thickness measurements.” *Ann. Glaciol.* 56(69):353-362.
- 748 Giles, K.A., S.W. Laxon, D.J. Wingham, D.W. Wallis, W.B. Krabill, C.J. Leuschen, D. McAdoo, S.S.
749 Manizade, and R.K. Raney. 2007. “Combined airborne laser and radar altimeter measurements over the
750 Fram Strait in May 2002.” *Rem. Sens. Env.* 111(2):182-194.
- 751 Gough, W.A., A.S. Gagnon, and H.P. Lau. 2004. “Interannual variability of Hudson Bay ice thickness.”
752 *Polar Geog.* 28(3):222-238.
- 753 Granskog, M.A., Z.Z.A. Kuzyk, K. Azetsu-Scott, and R.W. Macdonald. 2011. “Distributions of runoff,
754 sea-ice melt and brine using δ 18 O and salinity data—A new view on freshwater cycling in Hudson
755 Bay.” *J. Mar. Sys.* 88(3):362-374.

- 756 Hochheim, K.P and D.G. Barber. 2010. "Atmospheric forcing of sea ice in Hudson Bay during the fall
757 period, 1980-2005." *J. Geophys. Res.* 115:C05009.
- 758 Hochheim, K.P. and D.G. Barber. 2014. "An Update on the Ice Climatology of the Hudson Bay System."
759 *Arct. Antarct. Alp. Res.* 46(1):66-83.
- 760 Hochheim, H.P., J.V. Lukovich, and D.G. Barber. 2011. "Atmospheric forcing of sea ice in Hudson Bay
761 during the spring period, 1980–2005." *J. Mar. Sys.* 88:476-487.
- 762 Joly, S., S. Senneville, D. Caya, and F.J. Saucier. 2011. "Sensitivity of Hudson Bay sea ice and ocean
763 climate to atmospheric temperature forcing." *Clim. Dyn.* 36(9-10):1835-1849.
- 764 Kaleschke, L., X. Tian-Kunze, N. Maas, M. Makynen, and M. Drusch. 2012. "Sea ice thickness retrieval
765 from SMOS brightness temperatures during the Arctic freeze-up period." *Geophys. Res. Lett.* 39:L05501.
- 766 Kovacs, A. 1996. "Sea ice: Part II. Estimating the full-scale tensile, flexural, and compressive strength
767 of first-year ice." 96-11, Cold Reg. Res. and Eng. Lab., Hanover, NH.
- 768 Kurtz, N.T., N. Galin, and M. Studinger. 2014. "An improved CryoSat-2 sea ice freeboard retrieval
769 algorithm through the use of waveform fitting." *Cryosphere* 8:1217-1237.
- 770 Kwok, R. 2001. "Deformation of the Arctic ocean sea ice cover between November 1996 and April 1997:
771 a qualitative survey." Pp. 315-322 in *IUTAM symposium on scaling laws in ice mechanics and ice*
772 *dynamics*. Netherlands: Springer.
- 773 Kwok, R. 2005. "Variability of Nares Strait ice flux." *Geophys. Res. Lett.* 32:L234502.
- 774 Kwok, R. 2014. "Simulated effects of a snow layer on retrieval of CryoSat-2 sea ice freeboard." *Geophys.*
775 *Res. Lett.* 41:5014-5020.
- 776 Kwok, R. and G.F. Cunningham. 2008. "ICESat over Arctic sea ice: Estimation of snow depth and ice
777 thickness." *J. Geophys. Res.* 113:C08010.
- 778 Kwok, R. and G.F. Cunningham. 2015. "Variability of Arctic sea ice thickness and volume from Cryosat-
779 2." *Phil. Trans. R. Soc. A* 373(20140157).
- 780 Kwok, R., G.F. Cunningham, M. Wensnahan, I. Rigor, H.J. Zwally, and D. Yi. 2009. "Thinning and
781 volume loss of the Arctic Ocean sea ice cover: 2003–2008." *J. Geophys. Res.* 114:C07005.
- 782 Kwok, R., G.F. Cunningham, H.J. Zwally, and D. Yi. 2006. "ICESat over Arctic sea ice: Interpretation
783 of altimetric and reflectivity profiles." *J. Geophys. Res.* 111:C06006.
- 784 Kwok, R., G.F. Cunningham, H.J. Zwally, and D. Yi. 2007. "Ice, Cloud, and land Elevation Satellite
785 (ICESat) over Arctic sea ice: Retrieval of freeboard." *J. Geophys. Res.* 112:C12013.

- 786 Kwok, R. and D.A. Rothrock. 2009. "Decline in Arctic sea ice thickness from submarine and ICESat
787 records: 1958-2008." *Geophys. Res. Lett.* 36:L15501.
- 788 Lammers, R.B., A.I. Shiklomanov, C.J. Vörösmarty, B.M. Fekete, and B.J., Peterson. 2001. "Assessment
789 of contemporary Arctic river runoff based on observational discharge records." *J. Geophys. Res. Atmos.*
790 106(D4):3321-3334.
- 791 Landy, J., J. Ehn, M. Shields, and D. Barber. 2014. "Surface and melt pond evolution on landfast first-
792 year sea ice in the Canadian Arctic Archipelago." *J. Geophys. Res.* 119:3054-3075.
- 793 Laxon, S.W., K.A. Giles, A.L. Ridout, D.J. Wingham, R. Willat, R. Cullen, R. Kwok, A. Schweiger, J.
794 Zhang, C. Haas, et al. 2013. "CryoSat-2 estimates of Arctic sea ice thickness and volume." *Geophys.*
795 *Res. Lett.* 40:732-737.
- 796 Markus, T. and D.J. Cavalieri 1998. "Snow depth distribution over sea ice in the Southern Ocean from
797 satellite passive microwave data." Pp. 19-39 in *Antarctic Research Series, Antarctic Sea Ice: Physical*
798 *Processes, Interactions and Variability*, edited by M. O'Jefferies. Washington D.C.: American
799 Geophysical Union.
- 800 Markus, T., J. C. Stroeve, and J. Miller. 2009. "Recent changes in Arctic sea ice melt onset, freezeup,
801 and melt season length." *J. Geophys. Res.* 114:C12024.
- 802 Maslanik, J. A., C. Fowler, J. Stroeve, S. Drobot, J. Zwally, D. Yi, and W. Emery. 2007. "A younger,
803 thinner Arctic ice cover: Increased potential for rapid, extensive sea-ice loss." *Geophys. Res. Lett.*
804 34:L24501.
- 805 Maslanik, J. and J. Stroeve. 2016. "DMSP SSM/I-SSMIS Daily Polar Gridded Brightness Temperatures,
806 Version 4." Boulder, Colorado, USA.
- 807 Melling, H., Y. Gratton, and G. Ingram. 2001. "Ocean circulation within the North Water polynya of
808 Baffin Bay." *Atmos.-Ocean* 39:301-325.
- 809 Morison, J., R. Kwok, C. Peralta-Ferriz, M. Alkire, I. Rigor, R. Andersen, and M. Steele. 2012.
810 "Changing Arctic Ocean freshwater pathways." *Nature* 481:66-70.
- 811 Myers, R.A., S.A. Akenhead, and K. Drinkwater. 1990. "The influence of Hudson Bay runoff and ice-
812 melt on the salinity of the inner Newfoundland Shelf." *Atmos. Ocean* 28:241-256.
- 813 Parkinson, C.L. and D.J. Cavalieri. 2008. "Arctic sea ice variability and trends, 1979-2006." *J. Geophys.*
814 *Res.* 113:C07003.
- 815 April 2016. "The Integrated Arctic Corridors Framework."
- 816 Prinsenberg, S.J. 1988. "Ice-Cover and Ice-Ridge Contributions to the Freshwater Contents of Hudson
817 Bay and Foxe Basin." *Arctic* 41(1):6-11.

- 818 Regehr, E.V., N.J. Lunn, S.C. Amstrup, and I. Stirling. 2007. "Effects of Earlier Sea Ice Breakup on
819 Survival and Population Size of Polar Bears in Western Hudson Bay." *J. Wildlife. Man.* 71(8):2673-
820 2683.
- 821 Ricker, R., S. Hendricks, V. Helm, H. Skourup, and M. Davidson. 2014. "Sensitivity of CryoSat-2 Arctic
822 sea-ice freeboard and thickness on radar-waveform interpretation." *Cryosphere* 8:1607-1622.
- 823 Ryvlin, A. I. 1974. "Method of forecasting flexural strength of an ice cover." *Probl. Arct. Antarct.* 45:79-
824 86.
- 825 Saucier, F.J., S. Senneville, S. Prinsenberg, F. Roy, G. Smith, P. Gachon, D. Caya, and R. Laprise. 2004.
826 "Modelling the sea ice-ocean seasonal cycle in Hudson Bay, Foxe Basin and Hudson Strait, Canada."
827 *Clim. Dyn.* 23:202-326.
- 828 Schweiger, A., R. Lindsay, J. Zhang, M. Steele, H. Stern, and R. Kwok. 2011. "Uncertainty in modeled
829 Arctic sea ice volume." *J. Geophys. Res.* 116:C00D06.
- 830 Stern, H.L. and M.P. Heide-Jørgensen. 2003. "Trends and variability of sea ice in Baffin Bay and Davis
831 Strait, 1953–2001." *Polar Res.* 22(1):11-18.
- 832 Stewart, D.B. and D.G. Barber 2010. "The Ocean-Sea Ice-Atmosphere System of the Hudson Bay
833 Complex." Pp. 1-36 in *A Little Less Arctic: Top Predators in the World's Largest Northern Inland Sea,*
834 *Hudson Bay*, edited by S.H. Ferguson, L.L. Loseto, and ML. Mallory. New York: Springer.
- 835 Stewart, E.J., A. Tivy, S.E.L. Howell, J. Dawson, and D. Draper. 2010. "Cruise Tourism and Sea Ice in
836 Canada's Hudson Bay Region." *Arctic* 63(1):57-66.
- 837 St-Laurent, P., F. Straneo, J.F. Dumais, and D.G. Barber. 2011. "What is the fate of the river waters of
838 Hudson Bay?" *J. Mar. Sys.* 88(3):352-361.
- 839 Stroeve, J.C., T. Markus, L. Boisvert, J. Miller, and A. Barrett. 2014. "Changes in Arctic melt season
840 and implications for sea ice loss." *Geophys. Res. Lett.* 41:1216-1225.
- 841 Tang, C.C.L., C.K. Ross, T. Yao, B. Petrie, B.M. DeTracey, and E. Dunlap. 2004. "The circulation, water
842 masses and sea-ice of Baffin Bay." *Prog. Ocean.* 63:183-228.
- 843 Tian-Kunze, X., L. Kaleschke, and N. Maass. 2013, updated 2016. "SMOS Daily sea ice thickness [Nov
844 2010-Jan 2016]." Digital Media, ICDC, University of Hamburg, Hamburg, Germany.
- 845 Tian-Kunze, X., L. Kaleschke, N. Maaß, M. Mäkynen, N. Serra, M. Drusch, and T. Krumpfen. 2014.
846 "SMOS-derived thin sea ice thickness: algorithm baseline, product specifications and initial
847 verification." *Cryosphere* 8:997-1018.
- 848 Tilling, R.L., Ridout A., Shepherd A., and D.J. Wingham. 2015. "Increased Arctic sea ice volume after
849 anomalously low melting in 2013." *Nature Geoscience* 8:643-646.

- 850 Tschudi, M., C. Fowler, J. Maslanik, J.S. Stewart, and W. Meier. 2016. "Polar Pathfinder Daily 25 km
851 EASE-Grid Sea Ice Motion Vectors. Version 3." Boulder, Colorado USA.
- 852 Ulaby, F.T., R.K. Moore, and A.K. Fung. 1982. *Microwave Remote Sensing: Active and Passive*. Boston,
853 MA: Artech House.
- 854 Valeur, H.H., C. Hansen, K.Q. Hansen, L. Rasmussen, and N. Thingvad. 1996. "Weather, sea and ice
855 conditions in eastern Baffin Bay, offshore northwest Greenland, a review." Technical Report 96-12,
856 Danish Meteorological Institute.
- 857 Wang, J., L.A. Mysak, and R.G. Ingram. 1994. "Interannual variability of sea-ice cover in Hudson Bay,
858 Baffin Bay and the Labrador Sea." *Atmos. Ocean* 32:421-447.
- 859 Warren, S.G., I.G. Rigor, N. Untersteiner, V.F. Radionov, N.N. Bryazgin, and Y.I. Alexandrov. 1999.
860 "Snow Depth on Arctic Sea Ice." *J. Clim.* 12:1814-1828.
- 861 Wingham, D.J., C.R. Francis, S. Baker, C. Bouzinac, D. Brockley, R. Cullen, P. de Chateau-Thierry,
862 S.W. Laxon, U. Mallow, C. Mavrocordatos, and L. Phalippou. 2006. "CryoSat: A mission to determine
863 the fluctuations in Earth's land and marine ice fields." *Adv. Space Res.* 37(4):841-871.
- 864 Zwally, H. J., R. Schutz, C. Bentley, J. Bufton, T. Herring, J. Minster, J. Spinhirne, and T. Ross. 2014.
865 "GLAS/ICESat L2 Sea Ice Altimetry Data, Version 34." Boulder, Colorado. Retrieved June 2015.
- 866
- 867
- 868

869 **Figure 1.** Twelve sub-regions of the Eastern Canadian Arctic.

870 **Figure 2.** Temporal coverage of the different satellite datasets used in this study.

871 **Figure 3. (a)** Comparison between snow depth estimated from DMSP/SSMIS brightness temperatures
872 (used in this study) and estimated from AMSR-E brightness temperatures (provided by NSIDC), over
873 the concurrent period 2003-2009. **(b)** Histograms of annual mean snow depth from DMSP/SSMIS (blue)
874 and difference between AMSR-E and DMSP/SSMIS snow depths (red) for 2003-2009. **(c)**
875 ‘Climatological’ mean snow depth in spring (March-April), from DMSP/SSMIS brightness
876 temperatures, for 2003-2016. The bold line gives the mean ice edge (20% ice concentration).

877 **Figure 4. (a)** The areas where SMOS ice thickness data are utilized in November, December and January,
878 averaged over the period 2010-2016. **(b)** Comparison between distributions of ice thickness from SMOS
879 and Cryosat-2 within the transition zone in validity (0.8-1.3 m) between the two datasets.

880 **Figure 5. ‘Climatological’ (a)** mean sea ice thickness and **(c)** average uncertainty in thickness, as
881 observed by ICESat GLAS, Cryosat-2 and SMOS in November, and **(b)** mean sea ice thickness and **(d)**
882 average uncertainty in thickness, as observed by ICESat GLAS and Cryosat-2 in March, for 2003-2016.
883 Bold lines give the mean ice edge (20% ice concentration) for these periods.

884 **Figure 6.** Interannual variations in the east-west asymmetry of spring sea ice thickness in the Eastern
885 Canadian Arctic: **(a)** variations in the asymmetry parameter $d\bar{h}_i/dx$ in Hudson Bay and Baffin Bay from
886 2003 to 2016, and **(b)** asymmetries across the two bays in four years. Spatial anomalies of March ice
887 thickness in the Eastern Canadian Arctic with respect to the climatological average in **(c)** a close-to-
888 symmetrical year in Hudson Bay but asymmetrical year in Baffin Bay, 2007, and **(d)** a particularly

889 asymmetrical year in Hudson Bay but close-to-symmetrical year in Baffin Bay, 2014. Bold lines give the
890 mean ice edge (20% ice concentration).

891 **Figure 7.** Regional variations in the frequency distribution of sea ice thickness across the Eastern
892 Canadian Arctic in April 2014, superimposed on a composite of MODIS *Terra* images acquired on April
893 19th. The locations of persistent polynyas are indicated, including the Northwestern Hudson Bay Polynya
894 and the Northwater Polynya. Normalized frequency distributions of ice thickness have a 5-cm bin spacing
895 and the mean and modal ice thickness are given in purple and red, respectively.

896 **Figure 8.** Time-series of mean March sea ice thickness in the Eastern Canadian Arctic from 2003 to
897 2016, for the entire ECA and for groups of sub-regions separately. Error bars indicate one standard
898 deviation around the mean total ECA ice thickness. Linear trends are presented as separate dashed lines
899 for the mean ice thickness during ICESat and Cryosat-2 data periods..

900 **Figure 9.** Time-series of sea ice volume in the Eastern Canadian Arctic from 2003 to 2016. Ice volume
901 estimates for Nov-Jan 2010 to 2015 were obtained from combined Cryosat-2 and SMOS ice thickness
902 data.

903 **Figure 10. (a)** Mean sea ice motion and vorticity fields in the Eastern Canadian Arctic between January
904 and March 2014; relationship between vorticity ζ and the ice thickness asymmetry parameter $d\bar{h}_i/dx$ in
905 **(b)** Hudson Bay and **(c)** Baffin Bay, for the period 2003-2015.

906

907